Disclaimer

The report at hand was written in the course of the respective class at the University of Bonn. If not stated differently on top of the first page or the following website, the report was prepared and handed in solely by me, Marvin Zanke. Any handwritten annotations are usually corrections that I or a tutor made. For more information and all my material, check:
https://www.physics-and-stuff.com/

I raise no claim to correctness and completeness of the given report! This equally applies to the corrections mentioned above.

- Pre-lab questions: ok
- Introduction: ok
- Learning datasets: Event displays well described, assignments well done and well explained.
- Calibration: Well done but not very well described. You don't say which distribution you fit, which fit function you use and how you define the calibration factors.
- W mass: well done and well described.

Advanced Laboratory Course

E214: The ATLAS Experiment
(Porperties of W Bosons and the Search for New Physics)
Group P8

Marvin Zanke   Fabian Müller

s6mazank@uni-bonn.de   s6fnmuel@uni-bonn.de

September 25/26, 2018

Sub. on 3/10/2018

$\boxed{1.3}$

Contents

Abstract

In this experiment, we use $ATLAS$ data, in order to determine the $W^{\pm}$ boson mass. The experiment is carried out on two days.

On the first day, we use the event display of the program $ATLANTIS$ in order to identify different events in the detector. Here, we also looked at electron events specifically and determined their energy-over-momentum ratio as well as photon events to determine the conversion probability. Furthermore, we calibrated the electromagnetic calorimeter with data from the process $Z^0 \rightarrow e^- e^+$.

On the second day, we used simulated data and $ATLAS$ data in order to determine a gauge curve and the $W^{\pm}$ boson mass, using the $Jacobi\ peak$ method in the transverse momentum spectrum of the electron by looking at the decay $W^{\pm} \rightarrow e^{\pm} \overset{(-)}{\nu}_e$.

1 Theory

If not mentioned explicitly, the theory is based on the references [1] and [2].

1.1 Elementary Particles and the Standard Model

As far as we understand nowadays, most of the physics in our universe can be described with the help of a few *elementary particles*, collected in the so-called *standard model*, whose content is depicted in figure 1.1. Note here, that the gravitation is not taken into account because it is weak compared to the other forces. One easily verifies, that these elementary particles can be separated into *fermions* with spin $\frac{1}{2}$ and *bosons* with spin 1. The fermionic part is made up out of quarks and leptons – also referred to as the *matter content* – whereas the bosonic part is made up out of the vector bosons, mediating the electromagnetic-, weak-, and strong force between the particles and the higgs boson. As indicated in the figure, there exists an anti-particle for each particle, having the same mass but carrying the opposite charge. The whole theory is consistent only as a field theory of quanta, i.e. a quantum field theory.

Interactions in quantum field theories often rely on the principle of *local gauge invariance*. One promotes a global gauge symmetry of the Lagrangian to a local one and demands invariance, which in turn gives rise to the need of introducing gauge bosons. The gauge bosons couple to matter in (non-&)abelian-gauge theories and additionally to other gauge bosons in non-abelian gauge theories. Abelian and non-abelian refers to the underlying symmetry group and its generators here.

For the standard model, one chooses the most convenient and successful choice of an *electroweak unifying theory*, $SU(3)_\mathrm{C} \times SU(2)_\mathrm{L} \times U(1)_\mathrm{Y}$, where 'C' refers to color, 'L' to left-handed, 'Y' to the hypercharge. The first group then implies the existence of *eight gluons* and a coupling to particles carrying color, while the second group implies the existence of *three gauge bosons* (W^+, W^0, W^-) and a coupling to particles carrying weak charge. The third group gives rise to *one gauge boson B*
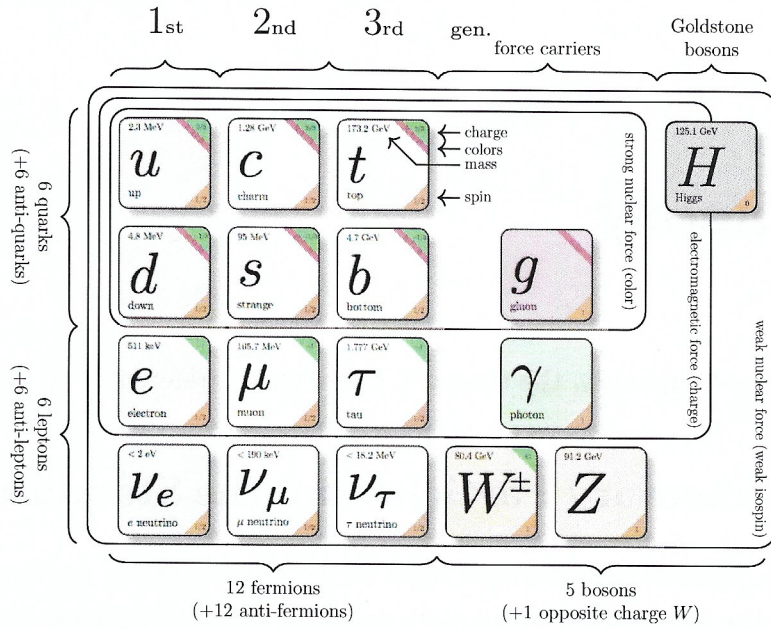
Figure 1.1.: The matter and gauge content of the Standard Model. (Code created in TikZ by Carsten Burgard, taken from [3], slightly edited for our purpose).

that couples via the hypercharge $Y = 2\left(Q - I_3\right)$, where Q is the charge and I_3 the third component of the weak isospin. The particles are here assumed to be written down as *doublets or singlets* under $SU(2)_\mathrm{L}$, e.g.

$$\begin{pmatrix} \nu_e \\ e^- \end{pmatrix}_\mathrm{L}, \qquad \begin{pmatrix} u \\ d \end{pmatrix}_\mathrm{L}$$

or

$$e^-_\mathrm{R}, \qquad u_\mathrm{R}, \qquad d_\mathrm{R}$$

respectively for the first generation. The color-indices are suppressed, as obviously, the quarks would consist of three different color-states. Note here, that right-handed neutrinos do not exist in the standard model and 'have to be' included via an extension as so-called physics beyond the standard model.

For reasons of consistency to experiments, the physical photon and Z^0 have to be a superposition of B and W^0 respectively, defining the *Weinberg angle* θ as the mixing angle for these. The gluons, as well as the W^+ and W^- are consistent with the physically observed bosons. Furthermore, the $SU(3)_\mathrm{C} \times SU(2)_\mathrm{L} \times U(1)_\mathrm{Y}$ gauge

group introduces three different couplings into the theory, which, after performing the change of basis indicated above, represent the electric charge e as the coupling constant of QED, the weak coupling and the strong coupling. With the help of the formalism of quantum field theory, one can show that the coupling of QED increases (decreases) with increasing (decreasing) momenta, while the strong coupling constant increases (decreases) with decreasing (increasing) momenta. This leads to the phenomenon of *asymptotic freedom*, stating that quarks behave like free particles for large probed energies, while they only appear in colorless bound states, being referred to as *confinement*. These color-neutral hadrons divide into mesons ($q\bar{q}$) and baryons (qqq) and form so-called *jets* when they are emitted as bundles in scatter or decay processes.

Up to this point, the gauge bosons are massless. A mass term for these would violate the gauge symmetry and is thus forbidden. Instead, one generates masses via the *higgs mechanism*. The group $SU(2)_{\mathrm{L}} \times U(1)_{\mathrm{Y}}$ is *spontaneously broken* to $U(1)_{\mathrm{em}}$ with the help of a complex higgs doublet (h^+, h^0) that acquires its *vacuum expectation value*, e.g. $(0, v)$. Note here that the four degrees of freedom from the initial higgs doublet are reduced to one and those three missing degrees of freedom are absorbed by three of the former massless gauge bosons – massive particles have an additional longitudinal polarization in contrast to massless ones. Consistent with Goldstone's theorem, we get one massless gauge boson which we identify with the photon and three massive, the (W^+, W^-) and Z^0. Some important properties as well as branching ratios of the Z^0 and W^- boson are collected in table 1.1 and table 1.2 respectively.

Property	Z^0 boson	W^- boson
electric charge [e]	0	−1
spin [$\hbar$]	1	1
decay width Γ_{tot} [GeV]	2.495 ± 0.002	2.141 ± 0.041
mass [GeV]	91.1876 ± 0.0021	80.403 ± 0.029

Table 1.1.: Properties of the Z^0 and W^- boson. The properties of the W^+ boson are identical to the W^- properties except for an opposite charge. Taken from [1].

Masses for fermions can be introduced via *Yukawa couplings*, which couple the higgs doublet to the fermions and give rise to mass terms after having the higgs doublet acquire its vacuum expectation value.

Z^0 boson		W^- boson	
decay	BR [%]	decay	BR [%]
$e^- e^+$	3.363 ± 0.004	$e^- \bar{\nu}_e$	10.75 ± 0.13
$\mu^- \mu^+$	3.366 ± 0.007	$\mu^- \bar{\nu}_\mu$	10.57 ± 0.15
$\tau^- \tau^+$	3.370 ± 0.008	$\tau^- \bar{\nu}_\tau$	11.25 ± 0.20
jets	69.91 ± 0.060	jets	67.60 ± 0.27
neutrinos	20.00 ± 0.060		

Table 1.2.: The branching ratios of Z^0 and W^- bosons, taken from [1]. The W^+ boson has the same branching ratios as the W^-.

This is of course only a short summary and presumes that the reader has some basic knowledge of those concepts. For more details, we can recommend the summary in [4, p. 161 et sqq.] on which this recap is partly based on. For a deeper understanding of quantum field theory, we refer to [5].

1.2 Relativistic Kinematics

Einstein's equation gives a relation between energy and mass in the form

$$E = mc^2.$$

A particle moving with the velocity v has the *energy and momentum*

$$E = \gamma mc^2 \qquad \text{and} \qquad \vec{p} = \gamma m\vec{v},$$

where

$$\gamma = \frac{1}{\sqrt{1 - \beta^2}} \qquad \text{and} \qquad \beta = \frac{v}{c}.$$

One also finds the relations

$$\gamma = \frac{E}{m} \qquad \text{and} \qquad \beta = \frac{|\vec{p}|}{E}.$$

Transformations from one coordinate system to another are described by *Lorentz transformations*.

1.3 Luminosity

Having obtained the experimentally observed event rates for a process, one is interested in calculating the cross section σ. This can be done with the help of the so-called *luminosity L*, which in turn only depends on the settings of the scattering experiment and can be obtained by simultaneously measuring the rate of another process with known cross section. For the event rate dn/dt, we then have

[handwritten: True, but it's not how we do it at the LHC.]

$$\frac{dn}{dt} = \sigma \cdot L,$$

or equivalently

$$n = \sigma \int L \, dt \tag{1.1}$$

with the integrated luminosity $\mathcal{L} = \int L \, dt$.

1.4 LHC and the ATLAS Experiment

The *Large Hadron Collider* (LHC) is a circular proton-proton accelerator at the CERN in Switzerland, where the protons originate from a hydrogen source and reach energies of $450\,\text{GeV}$ after a first acceleration. The LHC is installed $100\,m$ below ground in the old tunnel of the LEP accelerator. After being injected and further accelerated in the LHC ring, the *proton beams* are supposed to reach energies of $7\,\text{TeV}$. Two of those beams then *collide in a head-on collision* at a so-called interaction point, where there exist four such interaction points with one of them being named the *ATLAS* (experiment) (**A T**oroidal **LHC A**pparatu**S**). The energy in the center-of-mass frame is then $E_{\text{CM}} = \sqrt{s} = 14\,\text{TeV}$. Other experiments at the mentioned interaction points are called *ALICE, CMS and LHC-b*.

[handwritten left margin: There are many steps ...]

[handwritten left margin: ATLAS is a detector placed at the interaction point 1, called P1.]

1.4.1 Detector Components

Modern detector systems usually use combinations of *drift chambers* – to monitor the track and to measure the momentum of charged particles – and *calorimeters*, measuring the energy of charged and neutral particles.

[handwritten right margin: not only, we also have semiconductor detectors.]

The functionality of *drift chambers* is based on proportional counters, that is gas-filled volumes with positively charged wires. An electron liberated by ionization of an incoming charged particle will drift towards the wire. Due to the gain of energy in the electric field, an avalanche of electrons and ions will be created, leading to a

signal on the wire. Using *multi-wire proportional counters* and assuming a constant drift time, the trajectory of charged particles can be reconstructed by measuring the time difference between entry of the particle and response of the specific wire. Applying a magnetic field, the particles momentum can be measured from the curvature of the trajectory due to the *Lorentz force*.

In *calorimeters*, incoming particles deposit their energy via electromagnetic and strong interactions, leading to particle showers producing a proportional signal. They are often constructed in alternating layers of *dense absorbers* and *active detection devices* like scintillators.

Electrons passing matter create a *shower* by the combined effects of *bremsstrahlung and pair production*. Incoming or produced photons also lose their energy by *Compton scattering*. Reaching a *critical energy*, where the energy loss by bremsstahlung is equal to ionization, the shower stops. The *radiotion length* X_0 is an important characteristic of these showers. It describes the mean distance where the incoming electron only has $1/e$ of its initial energy.

Incoming hadrons produce showers by *inelastic nucleon collisions* until the shower hadrons are absorbed. The length of the shower is characterized by the *nuclear absorption length* λ_0, where the number of non-interacting hadrons is reduced to $1/e$. The nuclear absorption length is much larger than X_0.

For the purpose of a better identification, detectors consist of an *electromagnetic calorimeter (ECAL)* and thicker *hadronic calorimeter (HCAL)*, guaranteeing that the hadron's energy is completely absorbed.

1.4.2 Particle Identification

For the identification of the produced particles, the different detector systems are used.

Electrons (and positrons) can be observed in the *tracking system* and deposit their energy completely in the *ECAL*. Photons can not be tracked but are also completely absorbed in the *ECAL*. Hadrons only leave a small fraction of their energy in the *ECAL* and form wide clusters in the *HCAL*. → And they are seen in the tracker if they are charged.

Muons can be tracked, but do not form electromagnetic showers due to their high mass. Therefore, they have to be detected in *muon chambers*, outside of the calorimeters. Tauons decay either via $\tau^{\pm} \to l^{\pm} \overset{(-)}{\nu}_l \overset{(-)}{\nu}_\tau$ or into hadrons and a neutrino before leaving the beam pipe. The number of hadronic jets is small here and thus gives the possibility to identify the tauon. What do you mean?

Bottom quarks have a long lifetime and form regular jets.? B hadrons (hadrons

containing bottom quarks) decay inside the beam pipe, such that the innermost detector has to be adjusted for the identification. Top quarks decay into $W^+ b$ before they can form a jet and can thus be identified by three jets or one jet and a pair of lepton and neutrino.

Neutrinos only interact weakly and can not be detected directly. Here, the *missing transverse momentum* is used. How is it defined and measured?
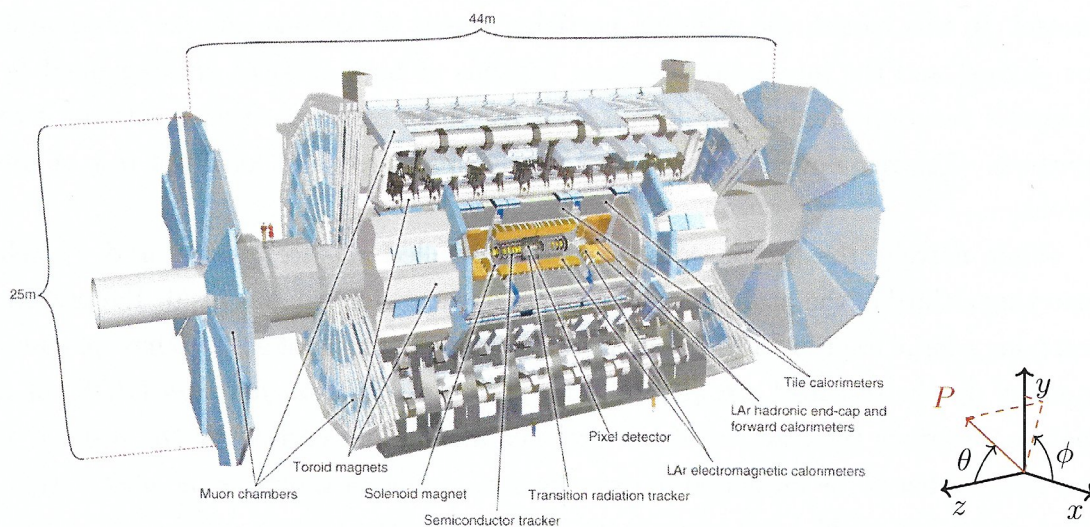
1.4.3 The ATLAS-Detector

Figure 1.2.: Structure of the ATLAS-detector. Taken from `http://science.sciencemag.org/content/338/6114/1576`. For the coordinate system, see `https://wiki.physik.uzh.ch/cms/latex:example_spherical_coordinates`.

The schematic structure of the ATLAS-detector is shown in figure 1.2. In the following, the important layers are described from inner, surrounding the collision point, to outermost.

The *pixel detector* is a silicon pixel detector, designed to give information on the primary interactions, especially on hadrons containing b-quarks. It is surrounded by the *semi-conductor tracker*, consisting of silicon microstrips, followed by the *transition radiation detector*, which is a drift chamber system measuring the particle's momenta and reconstructing the tracks. This inner detector is enclosed by a *solenoid*, producing a magnetic field of 2 T parallel to the beam axis for the inner detector.

This is followed by the calorimeter system, starting with a *presampler* helping to distinguish between single photons and photon pairs from π^0 decays. Since muons pass through the subsequent *ECAL* and *HCAL*, a *muon chamber* detects produced muons.

The coordinate system is defined as in figure 1.2. Instead of the *polar angle* θ, one often uses the *pseudo-rapidity* ... *why?*

$$\eta = -\ln\left(\tan\frac{\theta}{2}\right). \tag{1.2}$$

1.5 The Parton Model and Hadronic Collisions

High-energetic proton-proton collisions can be explained by the so-called *parton model*. In this model, the colliding particles consist of partons (quarks, antiquarks or gluons) and the interaction between hadrons at high energies are explained by inelastic reactions (called *hard scattering reactions* or *hard events*) between two partons. The remaining partons move nearly unaffected and form the rest of the event.

While naively, the proton consists of the so-called *valence quarks 'uud'* – each carrying a third of the proton's momentum – one also finds gluons inside the proton, carrying a large fraction of the momentum. These gluons might split up into $q\bar{q}$ pairs, making up the so-called *sea quarks*. The *parton distribution function* (PDF) of a parton describes the fraction of the proton's momentum carried by the respective parton and has to be measured in experiments. A rule of thumb is the observation, that about 1/6 of the total momentum is carried by the valence quarks.

In the following, we shall consider the hard scattering reaction $q\bar{q} \rightarrow gg$ with two produced jets as an example (following [1]). The possible Feynman graphs of the reaction can be seen in figure 1.3. ... *So? Why is this relevant here?*
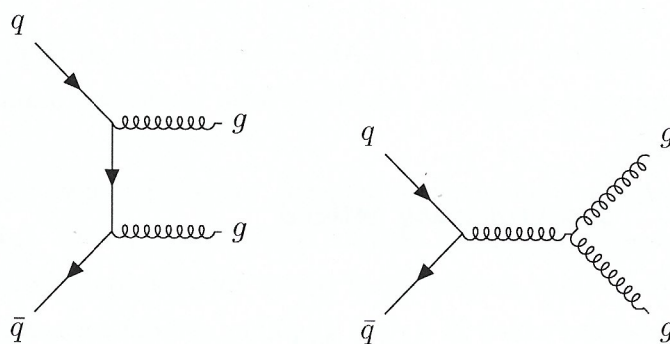

Figure 1.3.: Feynman graphs for the hard scattering process $q\bar{q} \rightarrow gg$, following [1].

As can be seen in figure 1.3, the quark of one proton interacts with an antiquark of the other proton, where the antiquark is created from a gluon radiated off from a quark. We will discuss this in detail for the *Drell-Yan process* in the next section. For now, let us assume that the two partons taking part in the hard reaction carry

the momentum fractions x_A and x_B before the reaction. The four-momenta then take the form

$$
p_A = \begin{pmatrix} E_{\text{beam}} \cdot x_A \\ 0 \\ 0 \\ E_{\text{beam}} \cdot x_A \end{pmatrix} \quad \text{and} \quad p_B = \begin{pmatrix} E_{\text{beam}} \cdot x_B \\ 0 \\ 0 \\ -E_{\text{beam}} \cdot x_B \end{pmatrix}.
$$

1.5.1 The Drell-Yan Process

The *Drell-Yan process* is an example of a hard reaction not based on QCD but QED. The Feynman graph is depicted in figure 1.4 and shows how a lepton pair is produced by the fusion of a quark-antiquark pair. Here, it also becomes clear, how
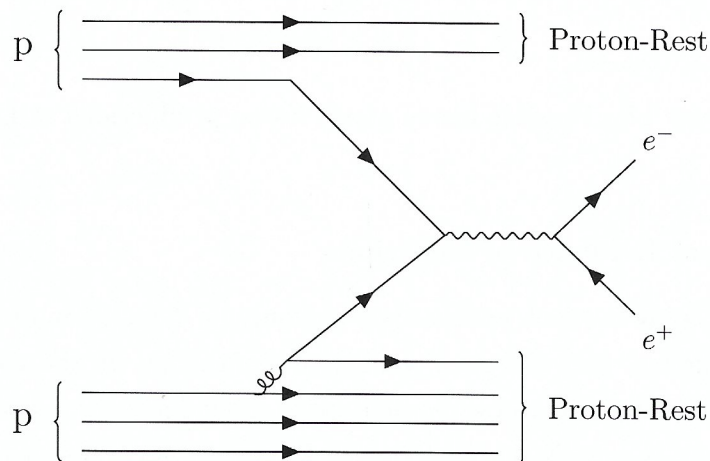

Figure 1.4.: Feynman diagram for the Drell-Yan process $pp \rightarrow e^- e^+$, created in TikZ following [1].

the antiquark is being created from the gluon-radiated off from one of the quarks. Analogously, there also exists a *weak Drell-Yan process* with a gauge boson of the weak interaction instead of the virtual photon.

1.6 Heavy Gauge Bosons

1.6.1 Heavy Gauge Boson at ATLAS

At the *LHC*, the heavy gauge bosons $W^\pm$ and Z^0 are produced by the interactions shown in figure 1.5, where the left process is the most important one, the so-called *weak Drell-Yan-process*. The gauge bosons mainly decay hadronically, which can not

be distuinguished from QCD background at *ATLAS*. For the Z^0 boson, the channels $Z^0 \to e^-e^+$ and $Z^0 \to \mu^-\mu^+$ are well reconstructable and the e^-e^+ channel will be used for the calibration of the detector in this experiment. *electromagnetic calorimeter measurements*

Furthermore, the $W^\pm$ boson can decay into a pair of lepton and neutrino. This channel will be used to determine the $W^\pm$ mass. The indirect detection of neutrinos will be discussed in the next section.
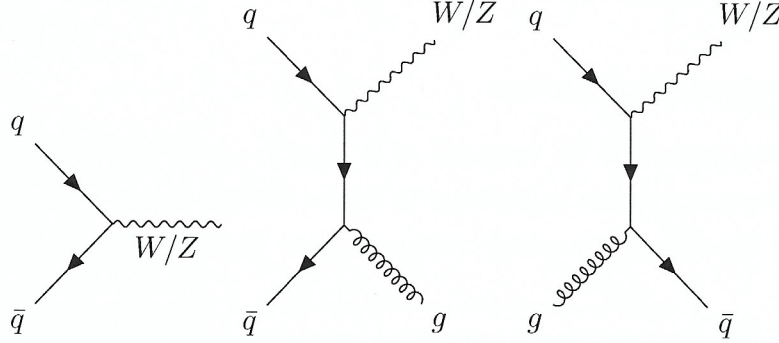
Figure 1.5.: Possible heavy gauge boson productions at LHC.

1.6.2 Indirect Evidence of Neutrinos

Since neutrinos only interact weakly, they can only be detected indirectly. Here, one makes use of the fact that the total transverse momentum (in the xy-plane) is zero. Thus, a non-zero total transverse momentum is an evidence for a weakly interacting particle. If there is exactly one neutrino in the event, its transverse momentum is given by

$$\vec{p}_T^{\,\nu} = -\sum_i \vec{p}_T^{\,i}. \tag{1.3}$$

In general, the *missing transverse energy* $\vec{\rlap{/}{E}}_T$ is defined as

$$\vec{\rlap{/}{E}}_T = -\sum_i E^i \sin\theta_i \, \vec{n}_{i,\perp}, \tag{1.4}$$

where E^i is the i-th energy entry in the calorimeter with the polar angle θ_i and $\vec{n}_{i,\perp}$ the unit vector pointing towards the energy entry in the xy-plane.

1.6.3 Jacobi Peak

To measure the $W^\pm$ boson mass, the *Jacobi peak* in the transverse momentum distribution of the electron – produced by $W^\pm \to e^\pm \overset{(-)}{\nu}_e$ – is used. In the $W^\pm$
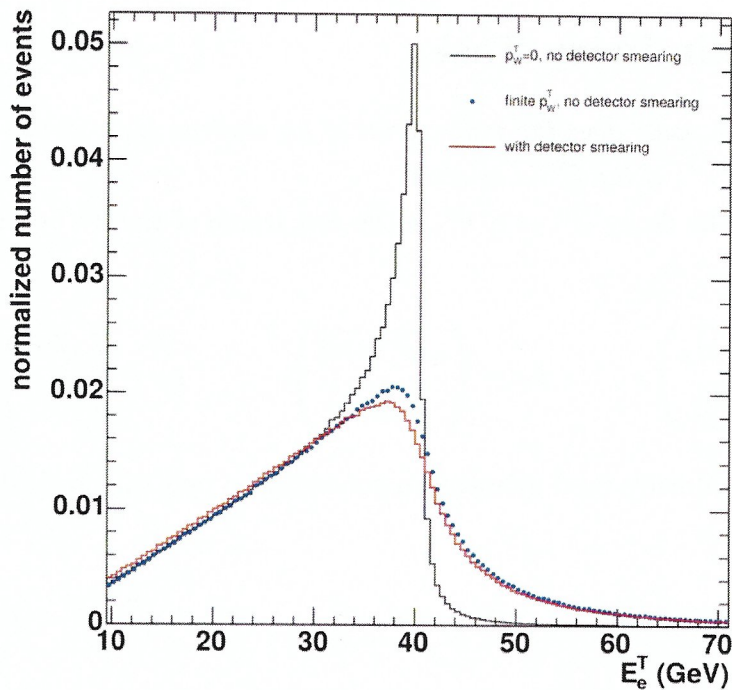
Figure 1.6.: The Jacobi Peak of the $W^\pm$ boson. Taken from [6].

boson's rest frame, the distribution of the electron's transverse momentum is given by

$$\frac{\mathrm{d}\sigma}{\mathrm{d}p_T} = \frac{\mathrm{d}\sigma}{\mathrm{d}\cos\theta^*}\frac{2p_T}{M_W}\frac{1}{\sqrt{\frac{1}{4}M_W^2 - p_T^2}}, \tag{1.5}$$

where θ^* is in reference to the incoming parton's axis. Since the transverse momentum is not affected by boosts in the beam direction, its distribution in the lab frame will only differ by $\mathrm{d}\sigma/\mathrm{d}\cos\theta^*$. Therefore, a pole at $p_T = M_W/2$ can be observed, the so-called *Jacobi peak*. This peak gets smeared by the $W^\pm$ boson's transverse momentum, its decay width and the detector resolution. This can be seen in figure 1.6.

1.7 Preliminary Tasks

7.2.2.A *Which value does the momentum of an electron have in the decay of a Z^0 boson $Z^0 \to e^- e^+$, if the Z^0 is at rest?*

Looking at the decay $Z^0 \to e^- e^+$ in the rest frame of the Z^0 boson, we find the four-momenta

$$p_Z = \begin{pmatrix} M_Z \\ 0 \end{pmatrix}, \qquad p_- = \begin{pmatrix} \sqrt{\vec{p}^2 + m_e^2} \\ \vec{p} \end{pmatrix}, \qquad p_+ = \begin{pmatrix} \sqrt{\vec{p}^2 + m_e^2} \\ -\vec{p} \end{pmatrix}.$$

Here, we have already used momentum conservation and the on-shell condition for the electrons, i.e.

$$p_Z = p_- + p_+ \qquad \text{and} \qquad p_\pm^2 = E^2 - \vec{p}^2 = m_e^2. \qquad (1.6)$$

Using momentum conservation once more, we find

$$M_Z = 2\sqrt{\vec{p}^2 + m_e^2}$$

and thus

$$|\vec{p}| = \sqrt{\frac{M_Z^2}{4} - m_e^2} = 45.595 \, \text{GeV}.$$

7.2.2.B *How large is the momentum of tau leptons in the reaction $e^- e^+ \to \tau^- \tau^+$, if the reaction takes place in the center-of-mass system (center-of-mass energy = 5 GeV)?*

Working in the center-of-mass system of the reaction $e^- e^+ \to \tau^- \tau^+$ and using momentum conservation as well as the on-shell condition from eq. (1.6), we find the four-momenta

$$p_1 = \begin{pmatrix} \sqrt{\vec{p}^2 + m_e^2} \\ \vec{p} \end{pmatrix}, \qquad p_2 = \begin{pmatrix} \sqrt{\vec{p}^2 + m_e^2} \\ -\vec{p} \end{pmatrix},$$

$$p_3 = \begin{pmatrix} \sqrt{\vec{q}^2 + m_\tau^2} \\ \vec{q} \end{pmatrix}, \qquad p_4 = \begin{pmatrix} \sqrt{\vec{q}^2 + m_\tau^2} \\ -\vec{q} \end{pmatrix}.$$

Here, p_1 and p_2 are referring to the electron and positron respectively, while p_3 and

p_4 refer to the τ^- and τ^+. The center-of-mass energy is given by

$$s = (p_1 + p_2)^2 = (p_3 + p_4)^2 = (5\,\text{GeV})^2,$$

such that we find

$$s = (p_3 + p_4)^2 = 4(\vec{q}^{\,2} + m_\tau^2)$$

and thus

$$|\vec{q}| = \sqrt{\frac{s}{4} - m_\tau^2} = 1.758\,\text{GeV}.$$

7.4.1.A *As before, the analysis is based on ROOT trees. One of the tree variables is ptw – the estimated transverse momentum of the W boson candidate. This variable can be constructed from the other tree variables. Please think about how this could be done. The tree variables are listed in section B.*

Using momentum conservation for the decay $W \to e\nu_e$, it is clear that

$$\vec{p}_T^{\,W} = \vec{p}_T^{\,e} + \vec{p}_T^{\,\nu}.$$

The variables for the electron's transverse momentum are `el_px` and `el_py`, while the transverse momentum of the neutrino is given by the missing transverse momentum `ptmisx` and `ptmisy`. The variable `ptw` seems to be the norm of that vector and can thus be written as

```
ptw = sqrt((el_px+ptmisx)**2 + (el_py+ptmisy)**2).
```

7.4.1.B *When fitting measurements to a linear function, the two parameters of a best fit straight line are y-intercept and slope. The errors on these parameters are typically correlated. Using these parameters for the error analysis will require a treatment that takes correlations into account. For example the simplest form of Gauss' error propagation law requires that the errors are uncorrelated. Please look up the correct form of the Gauss error propagation law in the presence of correlations. You will need that for the final error on the W mass.*
On the other hand, is it possible to minimize correlations by choosing an appropriate coordinate system?

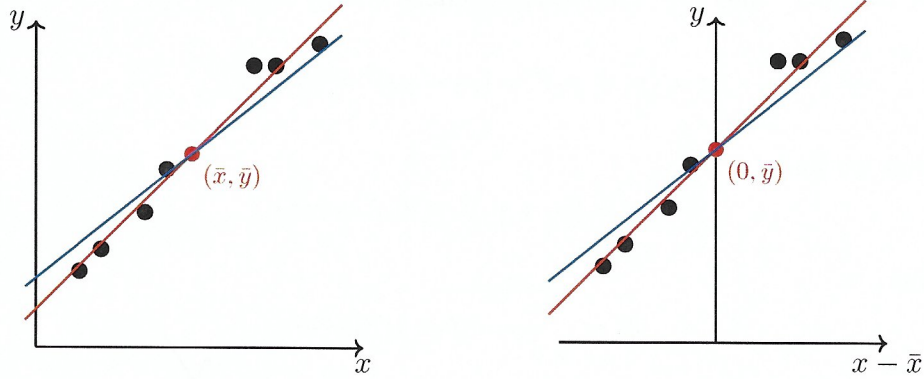The propagation of errors for a function f depending on the parameters $x =$

Figure 1.7.: Schematic procedure for the reduction of the correlation in a linear regression.

$(x_1, \ldots, x_n)$ is given by (cf. [8])

$$\sigma_f^2 = J^{\mathrm{T}} \Sigma_x J, \tag{1.7}$$

where Σ_x is the covariance matrix of $x = (x_1, \ldots, x_n)$ and J is the gradient of f.

In case of a linear function $f = mx + n$ ($\Rightarrow J = (x, 1)^{\mathrm{T}}$) with covariance matrix

$$\Sigma_x = \begin{pmatrix} \sigma_m^2 & \sigma_{mn} \\ \sigma_{mn} & \sigma_n^2 \end{pmatrix},$$

the error on f is given by

$$\sigma_f^2 = \sigma_m^2 x^2 + \sigma_n^2 + 2\sigma_{mn} x. \tag{1.8}$$

Slope and y-intercept are highly correlated in general and thus have a non-vanishing covariance σ_{mn}, as can be seen from figure 1.7 (left). A linear regression always intersects the point of (weighted) means $(\bar{x}, \bar{y})$, so that a change in the slope will lead to a change in the y-intercept and vice versa. This can be fixed by shifting the x-coordinate by $\bar{x}$, see figure 1.7 (right). ✓

7.5.1.A *What is the minimum invariant 4-lepton mass, when the four leptons originate from a Z^0 pair? Why do you find 4-lepton-events with invariant mass beneath this threshold?*

If the four leptons originate from a pair of real Z^0 bosons, their minimal invariant mass would be $2M_Z$. But there are also events, where either one or both of the Z^0 bosons are virtual, leading to a smaller invariant mass. ✓

7.5.1.B *Consider a Higgs boson which decays into two Z^0 bosons. How does the distribution of the 4-lepton-invariant-mass look like?*

The expected 4-lepton-invariant-mass distribution is a Breit-Wigner curve around the Higgs mass. $\sqrt{}$

7.5.1.C *Assume you have an ideal detector. What is the typical $\not{E}_T$ if a Z^0 pair has been produced and both Z^0 decay into electron or muon pairs? What $\not{E}_T$ will you expect when you have a real detector?*

In an ideal detector, all energy is deposited in the calorimeter, thus yielding $\not{E}_T = 0$. Real detectors have inefficiencies, leading to small values of $\not{E}_T$. $\checkmark$

7.5.1.D *The branching ratio of $t \to Wb$ is almost 100%. If you have a top anti-top pair in an event, both particles decay instantly via $t \to bW$. If both W bosons each decay leptonically ($W \to l\nu$), one finds two leptons in the event. What could explain the occurence of four leptons in a $t\bar{t}$ event?*

The b-quarks form B-mesons, which can decay leptonically or semileptonically. $\checkmark$

7.5.1.E *Do the following Gedanken-experiment: you create random integer numbers between 1 and 200. You record the occurence of each integer in a histogram with 200 bins. After histogramming 20,000 numbers, you expect an average 100 entries per bin. What is the statistical error for the number of entries in one bin? What is the probability of finding a bin with 130 entries? How many of such 130 entries bins (in average) do you expect to appear in 200 bins? In other words, what is the probability to find a deviation of 3 standard deviations in one of the bins of the distribution?*

The statistical error for the number of entries in one bin is $\sqrt{B} = \sqrt{100} = 10$. The number of excess events is $S = 130 - 100 = 30$, giving a significance of $S/\sqrt{B} = 3$. This corresponds to a probability of $p = 1 - 0.9973 = 0.0027$ and is an approximation to the precise result that can be obtained using the binomial distribution

$$p' = 1 - \sum_{k=0}^{129} \binom{20000}{k} \left(\frac{1}{200}\right)^k \left(1 - \frac{1}{200}\right)^{20000-k} = 0.0022.$$

So in average, one expects $N = 200p = 0.54$ bins with more than 129 entries. A simulation with 10000 randomly created histograms confirms the value from the binomial distribution $N = 0.44 = 200p'$.

2 Experimental Analysis

2.1 Experimental Setup

In order to be able to measure the $W^{\pm}$ boson mass on the second day of the experiment, we first familiarize with the graphic display of the program *ATLANTIS* on the first day. Here, we look at simulated data (so-called 'runs'), each containing several events with only a single particle simulated in the detector. We analyze the graphic display in order to be able to later identify particles in an unknown event. Furthermore, we calibrate the electromagnetic calorimeter on the first day. This is necessary, as the different detection modules of the calorimeter might vary in their energy yields (or even be defect) and electrons already lose energy before entering the calorimeter. To this end, we use an electron sample data set and apply an iterative energy calibration.

$Z \to e^+e^-$

On the second day, we apply the found energy calibration onto *ATLAS* data for the decay of a $W^{\pm}$ boson. We look at the channel $W^{\pm} \to e^{\pm} \overset{(-)}{\nu}_e$ and use the *Jacobi peak* method to determine the mass of the $W^{\pm}$ boson.

2.2 Part 1: Graphic Display of Particle Reactions

In the first part of this experiment, we use the program *ATLANTIS* in order to graphically display particle reactions. With the help of *ATLANTIS*, tracks of electrically charged particles in the inner detectors, and muon chambers as well as the energy disposal of charged and strongly interacting particles in the ECAL and HCAL can be displayed. To get started, one enters the following commands in a terminal

```
skitathena -r 12.0.7
java -jar atlantis.jar
```

and then loads a data set from 'Files/Read Event'.

2.2.1 Particle Identification

We successively load the five 'learning' data sets for electrons, muons, photons, tauons and jets to take a look at some of the contained events. The desired data sets do either carry the prefix 'single' or are called 'dijets' for the jet data set.

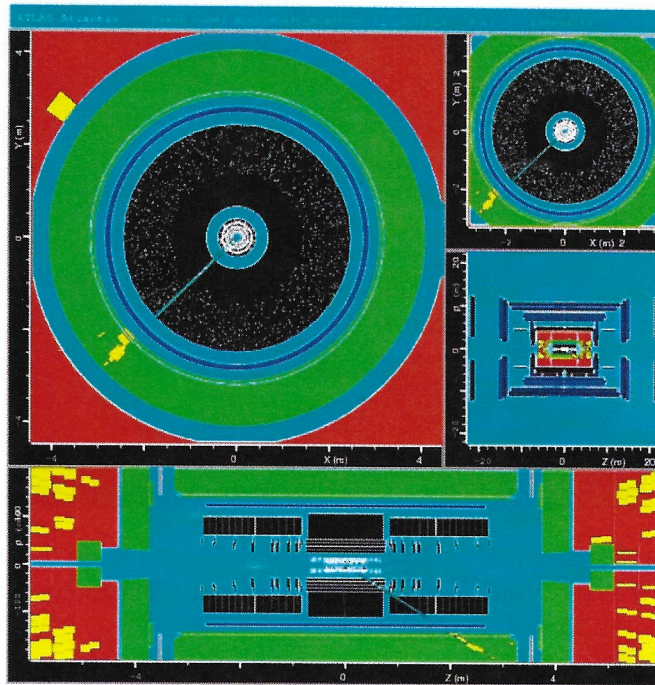Starting with the electron data set, one event is generically shown in figure 2.1.

Figure 2.1.: Inner detector: $P = -89.35\,\text{GeV}$ and $P_T = -(50.87 \pm 1.34)\,\text{GeV}$. ECAL: $E = 86.5\,\text{GeV}$ and $E_T = 49.2\,\text{GeV}$.

Looking at the cross section view in the upper left part of the screen, one clearly sees the track of a particle (the electron, teal line) in the inner detector (black area) and an energy disposal (yellow boxes) in the ECAL (green area). While there is no energy deposited in the HCAL (red area) originating from the said particle, there is some energy deposited in the upper left corner. This can either be ascribed to rests of the foregone proton-proton collision or to other background effects. Same holds true for the energy disposal in the hadronic calorimeter visible in the frontal view at the bottom of the screen. Without zooming in, one expects the muon chamber outside of the hadronic calorimeter in the cross section view. In our case, there was nothing registered. The caption beneath the figure shows the momentum P, as well as the transverse momentum P_T measured in the inner detector and the energy E, as well as the transversal energy E_T measured in the ECAL. Note, that the momentum P of the particle in the inner detector and the energy in the ECAL are approximately equal. We will discuss this in detail in 2.2.2. ✓

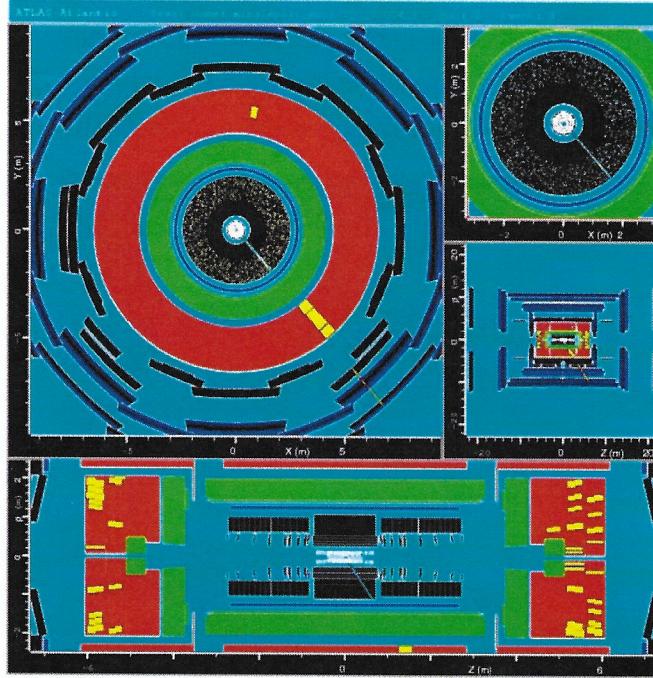Analogously, one finds figure 2.2 for the muon learning data set.

Figure 2.2.: Inner detector: $P = 48.89\,\text{GeV}$ and $P_T = (41.96 \pm 0.83)\,\text{GeV}$. HCAL: $E = 2.8\,\text{GeV}$ and $E_T = 2.2\,\text{GeV}$. Muon Chamber: $P = 44.77\,\text{GeV}$ and $P_T = (38.11 \pm 1.33)\,\text{GeV}$

We also see the expected track in the inner detector, but no energy disposal in the ECAL because of the high mass of the muons (almost no bremsstrahlung). Instead, there is some energy deposited in the HCAL. Characteristic for a muon, we see a particle track in the muon chamber (outermost, blue area). Additionally to the momentum and transverse momentum in the inner detector, the caption beneath the figure gives the momentum P, as well as the transverse momentum P_T measured in the muon chamber and the energies E and E_T measured in the HCAL instead of the ECAL.

For the photon learning data set, we find figure 2.3. What's characteristically here is, that we do not see the track of a particle in the inner detector, but measure an energy disposal in the ECAL. The energy deposited in the HCAL does not belong to the photon event and there is also no track visible in the muon chamber. The caption beneath the figure again gives an overview of the relevant variables.

An example of an event from the tauon learning data set is shown in figure 2.4. The particle track visible in the inner detector does not represent a tauon, but rather another charged particle originating from the heavy and thus fast decaying tauon.
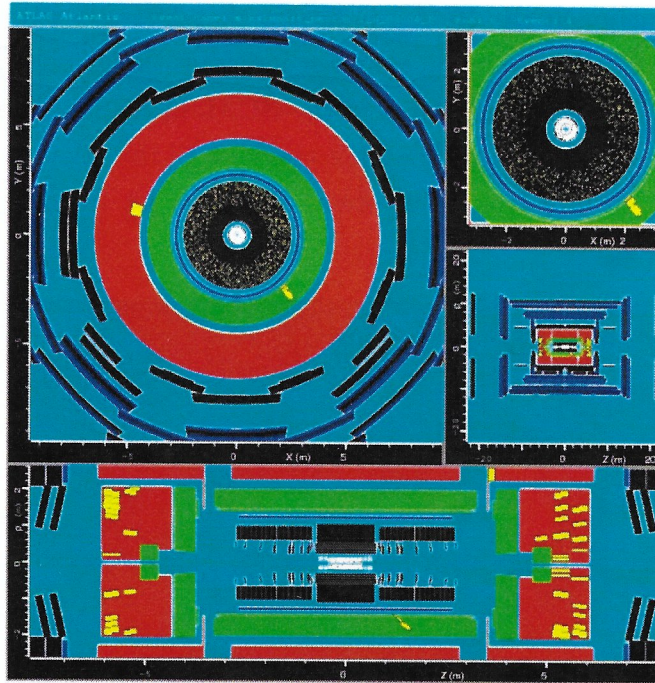
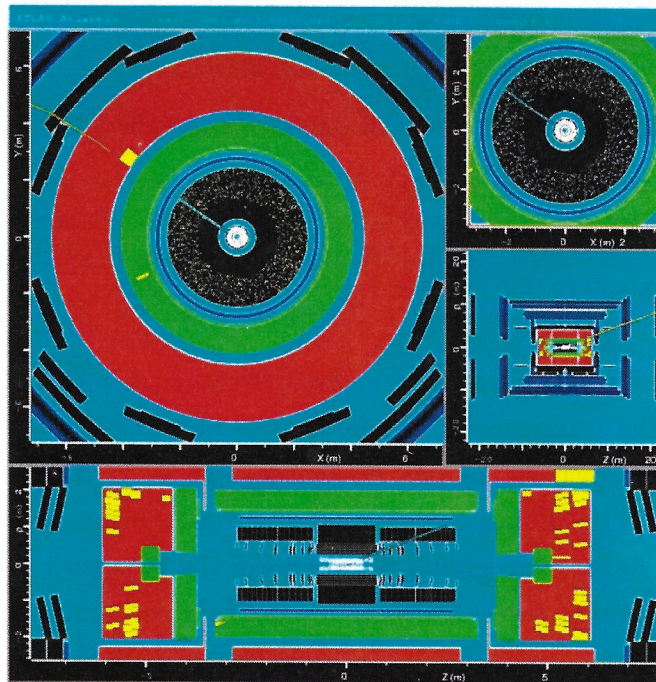Figure 2.3.: ECAL: $E = 47.5\,\text{GeV}$ and $E_T = 35.7\,\text{GeV}$.

Figure 2.4.: Inner detector: $P = 15.2\,\text{GeV}$ and $P_T = (5.99 \pm 0.15)\,\text{GeV}$. HCAL: $E = 0.96\,\text{GeV}$ and $E_T = 0.39\,\text{GeV}$. Muon Chamber: $P = 12.34\,\text{GeV}$ and $P_T = (4.77 \pm 0.21)\,\text{GeV}$.

The deposited energy in the HCAL indicates that hadrons were involved in this decay, while the track in the muon chamber indicates the involvement of muons (in consistency with the energy deposited in the HCAL in the muon learning data set). The caption beneath the figure shows the overview of the relevant variables again.

The last event we are looking at stems from the jet learning data set and is depicted in figure 2.5.
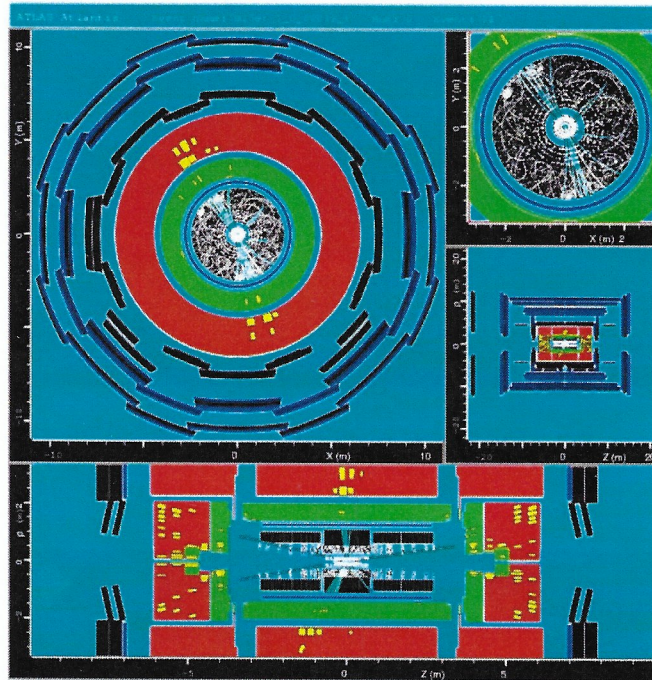
There are no hadrons, it's

$\tau \to \mu \nu_\tau \nu_\mu$

Figure 2.5.: Due to the large amount of particle tracks, we desist from giving the values of the variables as usual. But for most of the events we looked at, the energy deposited in the ECAL is smaller than the energy deposited in the HCAL.

Clearly visible are the many tracks in the inner detector, stemming from the hadronic showers due to the confinement of quarks. As quarks are charged particles, we measure an energy disposal in the ECAL, as well as in the HCAL. We do not measure a track in the muon chamber, as there are no muons in the event. For this data set, we desist from giving the values of the momenta and energies in the inner detector and calorimeters, as we would not be able to reasonably ascribe these values to the corresponding particle tracks. What we can note here is, that there is more energy deposited in the HCAL than in the ECAL.

Having discussed this part on the graphic display and identification of particles, we get to the assignments. We chose to work on assignment 2 and assignment 4.

2.2.2   Assignment 2 and 4

In assignment 2, we were supposed to load the electron learning data set from before and determine the momentum of the electron track in the inner detector, as well as the energy of the clusters in the ECAL for twenty events. Setting up a table, we were then supposed to calculate the ratio of the cluster energy and electron momentum and make a histogram of the result. Said table is depicted in table 2.1. We skipped events where there was more than one track visible in the inner detector, as the data set was supposed to only contain single electrons. ✓

Event no.	Momentum P [GeV]	Energy E [GeV]	$|E/P|$
1	−26.20	54.70	2.09
2	22.78	35.20	1.55
3	−244.34	223.20	0.91
6	66.67	78.30	1.17
8	129.82	162.90	1.25
9	−3.27	47.70	14.59
10	79.01	66.20	0.84
11	−95.93	78.70	0.82
12	37.40	30.60	0.82
13	−89.35	86.50	0.97
14	235.24	242.30	1.03
15	−105.14	105.30	1.00
17	−28.62	28.10	0.98
18	53.41	46.40	0.87
19	−32.92	64.30	1.95
20	105.64	80.80	0.76
22	93.52	82.10	0.88
23	−113.98	92.70	0.81
24	155.35	283.00	1.82
25	−36.40	33.80	0.93

Table 2.1.: The momentum of the electron tracks in the inner detector, as well as the energy of the clusters in the ECAL and the calculated ratio of energy and momentum for twenty events of the electron learning data set. We skipped events with more than one track in the inner detector.

Making a histogram for the frequency of the ratios $|E/P|$ with the help of table 2.1, we find figure 2.6 with an observable peak at $|E/P| = 0.8$. In the histogram, we left out the event no. 9 with a large ratio, which we ascribe to either a measuring error

or a falsely assigned photon event. What one would expect is a peak at $|E/P| \lesssim 1$ because of the small energy loss in the inner detector. ✓
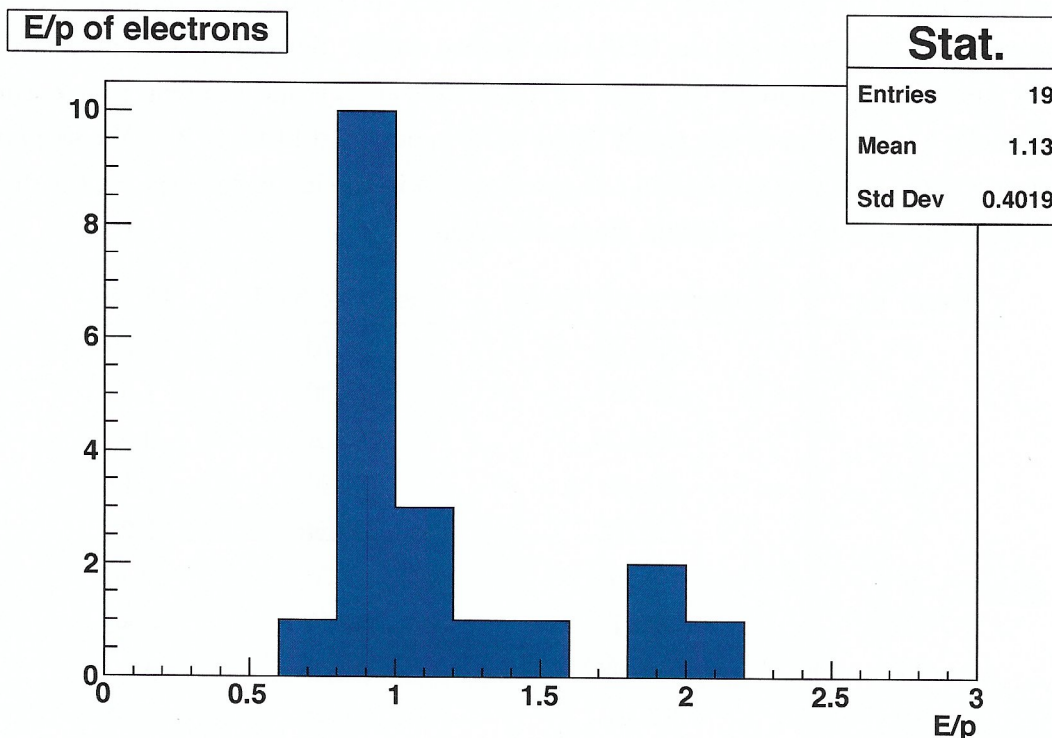

Figure 2.6.: The histogram for the ratio $|E/P|$, created with the help of table 2.1. Observable is the clear peak at $|E/P| = 0.8$.

In assignment 4, we were supposed to determine the photon conversion probability. To that end, the single photon learning sample with a total number of 50 events was used. Events with a converted photon are easily identified by visible tracks in the inner detector.

The observed tracks came in a multiplicity of either one or two and deposited their whole energy in the ECAL. It can be concluded, that the photons produced electron-positron pairs, which is the most likely process to happen because of the low $e^{\pm}$ mass. In total, nine such events were found, which are listed in table 2.2. Note here, that we did not keep the events without tracks, i.e. all event numbers between 0 and 49 that are not listed did not show a track.

All photons were converted inside the beam pipe, the primary vertex could be located in a range of $\sim 100\,\mu$m up to $\sim 1\,$mm from the center. As an example, the zoomed view of the graphical display for one event is shown in figure 2.7.

From table 2.2, the conversion probability of photons up to a range of a few mm

Event no.	#Tracks	Energy [GeV]	η	Ann.
2	2	39.1	-1.0	$\sim 1\,mm$
5	1	285.6	-2.5	$\sim 100\,\mu m$
8	1	89.2	2.5	$\sim 1\,mm$
22	2	123.0	1.8	$\sim 1\,mm$
23	2	196.2	2.3	$\sim 1\,mm$
28	1	97.8	-1.8	$\sim 1\,mm$
29	1	162.5	2.2	$\sim 1\,mm$
37	2	77.5	1.2	$\sim 1\,mm$
47	2	212.0	2.1	$\sim 1\,mm$

Table 2.2.: The found tracks and measured energies in the ECAL for the events in the photon learning data set, as well as the corresponding pseudo-rapidity η. As an annotation, we added the range from the center, where the conversion took place.
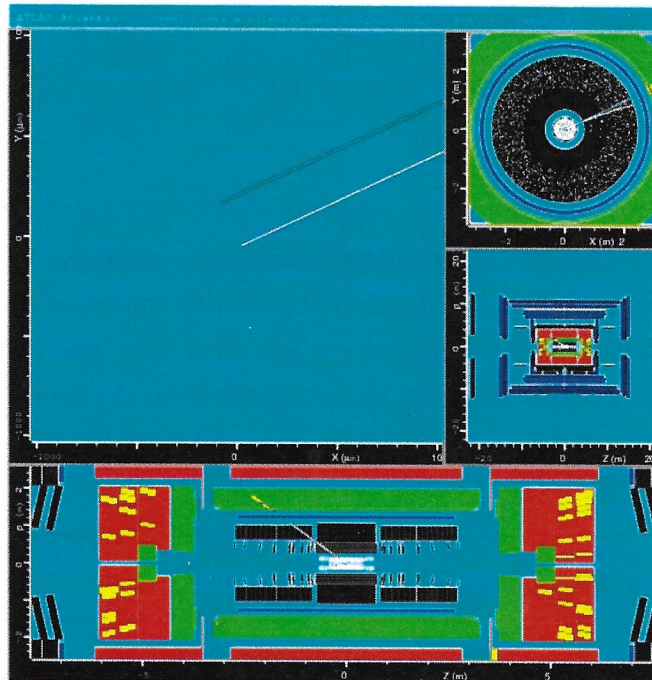
Figure 2.7.: Typical photon conversion event with two tracks. The X and Y scale in the upper-left is -1000 μm to -100 μm.

can be estimated by

$$P_{\gamma\text{-conv}} \sim 0.18.$$

The appearance of just one track could be explained by an almost collinear electron-positron pair that could not be resolved. It was expected that more energetic events or/and high $|\eta|$ produce these collinear tracks, but a correlation as tried to find in table 2.2 could not be found.

2.3   Part 2: Calibration of Electrons

As a calorimeter consists of hundreds of modules with slightly varying energy yields, the energy measurement has to be calibrated. Further reasons for the calibration are systematic losses by inactive (defect) regions and energy losses by the electron before entering the calorimeter (due to variable distances). For the energy calibration, we measure the distribution of electron-positron pairs created in the decay process of a Z^0 boson and make use of the data-analysis program $ROOT$ to perform all fits and display the distributions.

We start by typing the following commands from the home directory in a terminal:

```
source studentchoice WMASS
cd ZeeFit
source setup.sh
.L fitZee.C+
fitZee.z
```

These commands setup $ROOT$ with the choice to measure the $W^\pm$ boson mass on the second day and initialize a calibration object with the name 'z'. This object will be used for the calibration. Additionally, a so-called 'tree' has been created, which contains information about electrons and positrons from the decay of Z^0 bosons and can be accessed by e.g.

```
tree->Draw("Variable","Cut")
```

with the second input being optional. Using the method

```
z.Fit("")
```

we can fit the Z^0 peak to all e^-e^+-pairs in the data set. Note here, that $ROOT$ chooses only part of the data set to perform the fit, which will be of importance later as we have to use an iterative procedure to calibrate the energy measurement. We are also able to only look at events passing a certain cut, e.g.

```
z.Fit("el_eta<2.5 && el_eta>2.25")
```

fitting the Z^0 peak only [*full range*] to the electrons in a range of $\eta \in (2.25, 2.5)$. Without changing the calibration file, the distribution looks like depicted in figure 2.8, with the mass of the Z^0 boson being below its nominal value of $M_Z = 91.19 \, \text{GeV}$ and the resolution being in the same range as the decay width of the Z^0 boson.
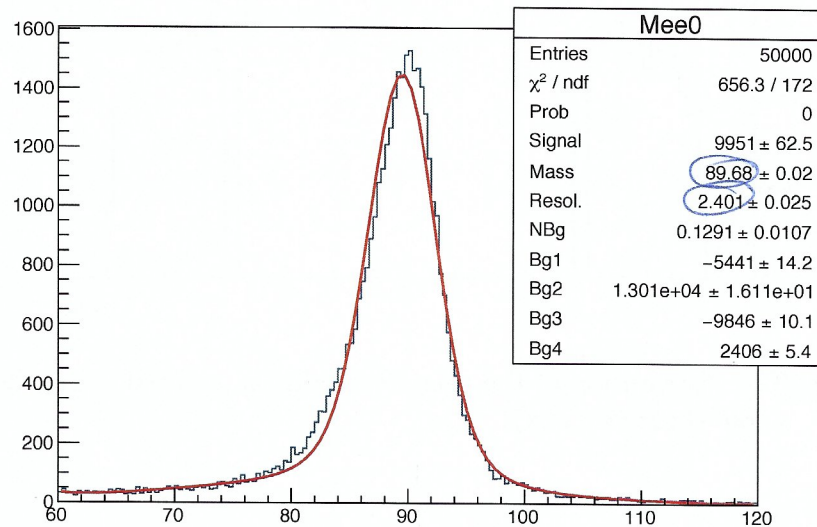

MeeO	
Entries	50000
χ^2 / ndf	656.3 / 172
Prob	0
Signal	9951 ± 62.5
Mass	89.68 ± 0.02
Resol.	2.401 ± 0.025
NBg	0.1291 ± 0.0107
Bg1	-5441 ± 14.2
Bg2	$1.301\text{e}+04 \pm 1.611\text{e}+01$
Bg3	-9846 ± 10.1
Bg4	2406 ± 5.4

Figure 2.8.: The distribution of the energy measured in the ECAL without changing the calibration file.

[*Why is it so important?*]

We focussed on the pseudo-rapidity η first. The distribution of this variable is depicted in figure 2.9.

We divided the interval $(-2.5, 2.5)$ into subintervals of size $|0.25|$ (with some exceptions in the regions with almost no events) and looked at the fitted Z^0 peak in these regions using the fit command with cuts mentioned above. Having worked through the whole interval for the first time, we find a factor for the energy correction in the different intervals of the pseudo-rapidity η and the distribution as depicted in figure 2.10. [*How is the correction factor derived?*]

We notice that the mass gives a better approximation of the nominal Z^0 bosons mass now, being slightly above this value. The resolution improved slightly. As [*Numbers?*] mentioned earlier, *ROOT* chooses only part of the data set to perform the fits, such that after rerunning the fits for the same data set, we yet acquire a different Z^0 boson mass. We thus repeat the procedure for the same intervals and once more apply a correction factor for the energy measurement, arriving at 2.11.
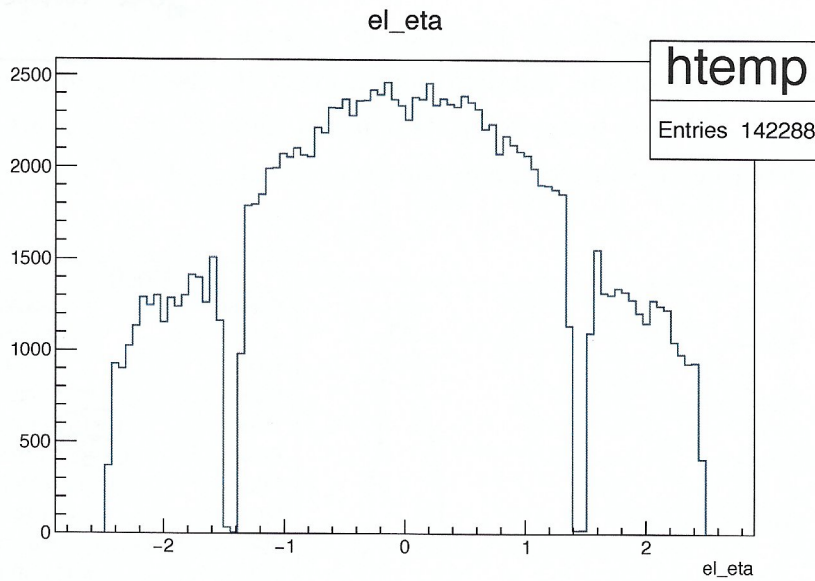
Figure 2.9.: The distribution of the pseudo-rapidity η, created using the command tree→Draw(el_eta).
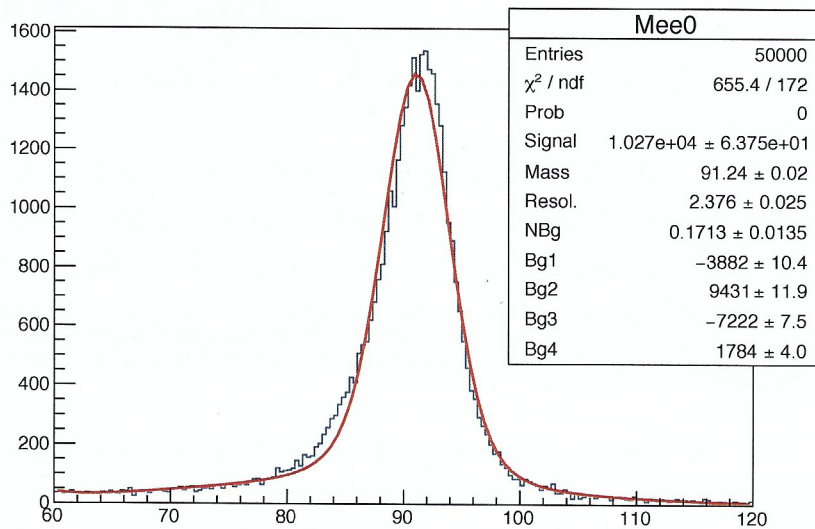

Figure 2.10.: The distribution of the energy measured in the ECAL with the first ~~cuts~~ *corrections* applied to the pseudo-rapidity in the calibration file.
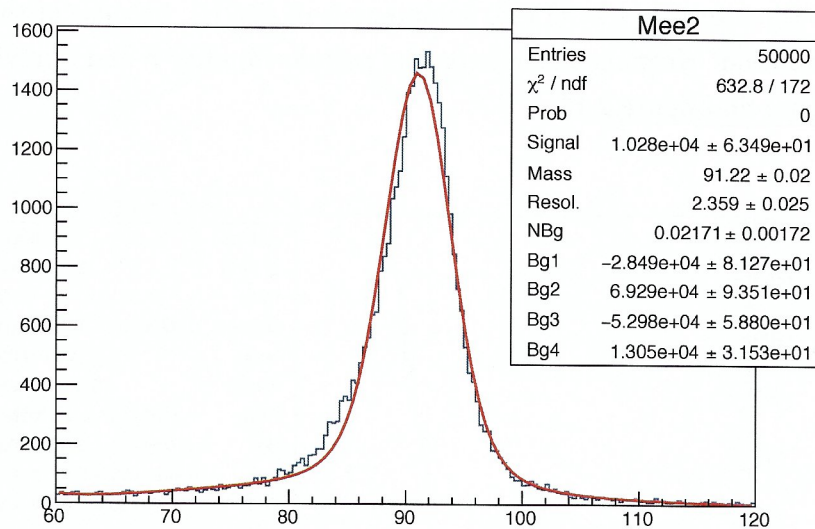
Figure 2.11.: The distribution of the energy measured in the ECAL with the second ~~cuts~~ *corrections* applied to the pseudo-rapidity in the calibration file.

We see another improvement of the approximated Z^0 boson mass, being only slightly out of the error range of the nominal Z^0 boson mass. Furthermore, the resolution ~~increased~~ *improved* slightly.

Turning to the azimuth angle ϕ now, we repeat the above procedure for this variable, where the distribution of the variable is given in figure 2.12.
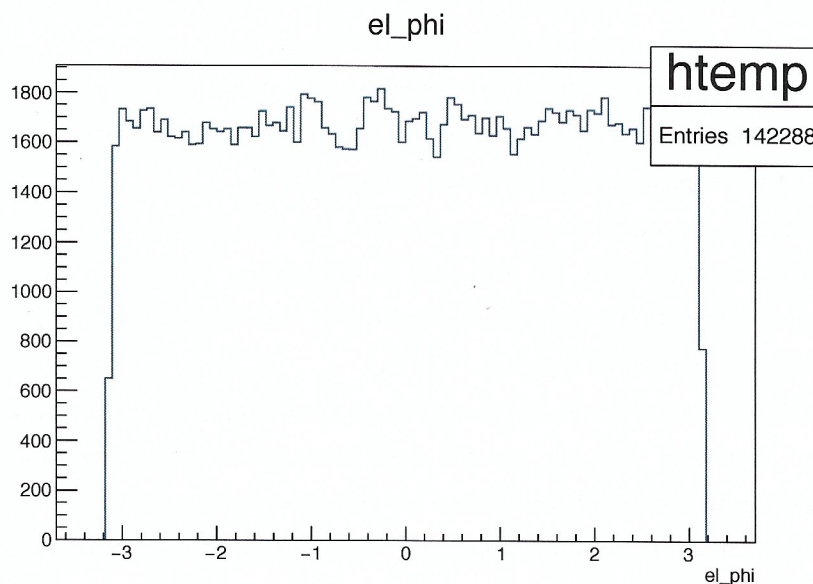
Figure 2.12.: The distribution of the azimuth angle ϕ, created using the command $tree \rightarrow Draw(el\_phi)$.

31

We divide the interval $(-\pi, \pi)$ into subintervals of size $|1|$, because of the homogeneous distribution. Keeping the cuts on the pseudo-rapidity η and applying the first cuts on ϕ, we find figure 2.13.

MeeO	
Entries	50000
χ^2 / ndf	622.7 / 172
Prob	0
Signal	1.028e+04 ± 6.465e+01
Mass	91.17 ± 0.02
Resol.	2.357 ± 0.025
NBg	0.001497 ± 0.000164
Bg1	−4.075e+05 ± 3.090e+03
Bg2	9.908e+05 ± 3.347e+03
Bg3	−7.569e+05 ± 1.673e+03
Bg4	1.863e+05 ± 1.588e+03
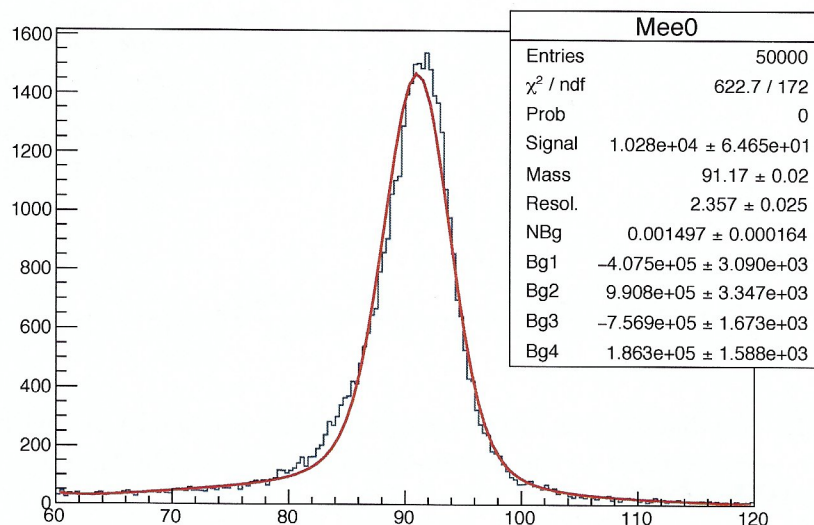
Figure 2.13.: The distribution of the energy measured in the ECAL with the first cuts applied to the azimuth angle in the calibration file.

The approximated mass of the Z^0 boson now lies in the 1σ confidence level of the nominal Z^0 boson mass and the resolution increased slightly again. Doing the calibration with ϕ for a second time, we find figure 2.14.
While the approximated mass did not change, the resolution slightly improved.

As a last step of the calibration, we focussed on the transverse momentum P_T, with the distribution looking like given in figure 2.15.
For the transverse momentum P_T, we divided the interval $(0, 150)$ into subintervals of different sizes ($|20|$, $|10|$, $|5|$ and $|\inf|$), depending on the amount of available data. Keeping the cuts on the pseudo-rapidity η and the azimuth angle ϕ, we apply the first cuts on P_T to find figure 2.16.
Repeating this procedure and applying the second cuts, we find figure 2.17. For the later course of action, we only use the first iteration on the transverse momentum due to a decline in the resulting values for the second iteration.

Our final calibration file containing all the mentioned steps can be found in appendix A.

$\longrightarrow$ *Final numbers that you get? You should report them and comment them.*
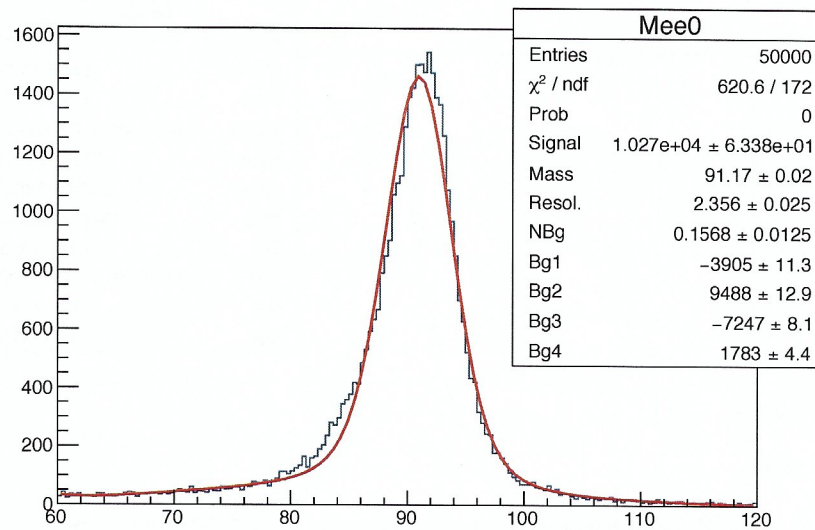
Figure 2.14.: The distribution of the energy measured in the ECAL with the second cuts applied to the azimuth angle in the calibration file.
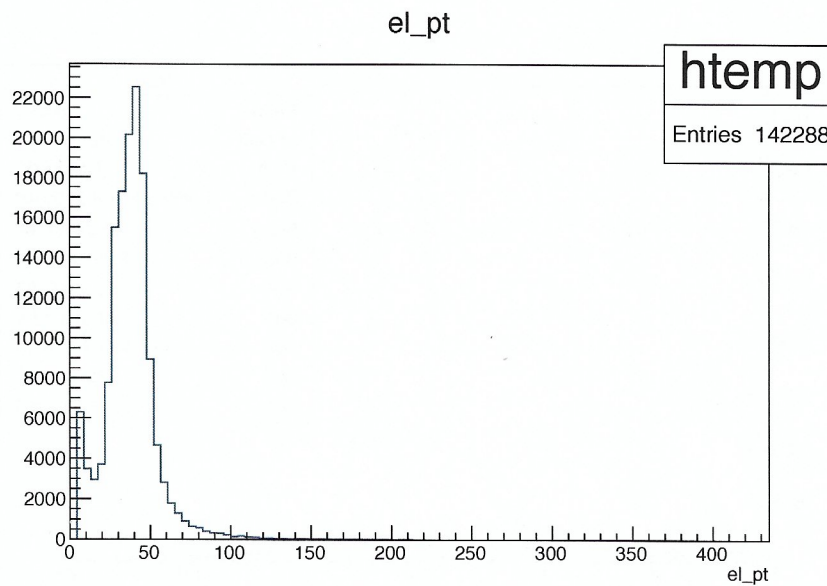

Figure 2.15.: The distribution of the transversal momentum P_T, created using the command $tree{\to}Draw(el\_pt)$.
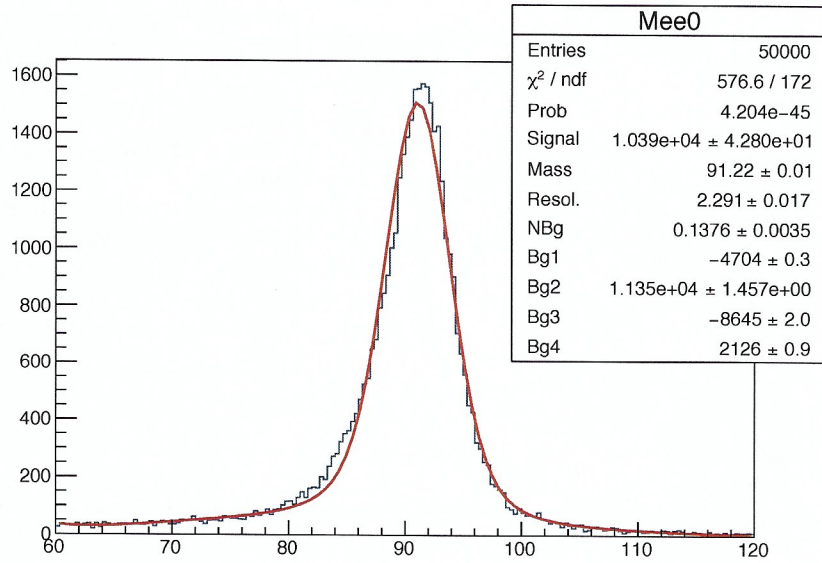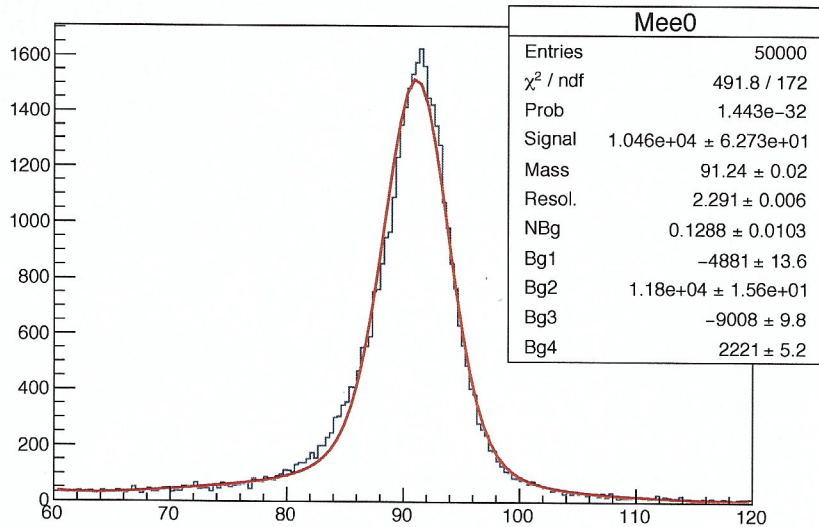
Mee0	
Entries	50000
χ^2 / ndf	576.6 / 172
Prob	4.204e−45
Signal	1.039e+04 ± 4.280e+01
Mass	91.22 ± 0.01
Resol.	2.291 ± 0.017
NBg	0.1376 ± 0.0035
Bg1	−4704 ± 0.3
Bg2	1.135e+04 ± 1.457e+00
Bg3	−8645 ± 2.0
Bg4	2126 ± 0.9

Figure 2.16.: The distribution of the energy measured in the ECAL with the first cuts applied to the transverse momentum in the calibration file.

Mee0	
Entries	50000
χ^2 / ndf	491.8 / 172
Prob	1.443e−32
Signal	1.046e+04 ± 6.273e+01
Mass	91.24 ± 0.02
Resol.	2.291 ± 0.006
NBg	0.1288 ± 0.0103
Bg1	−4881 ± 13.6
Bg2	1.18e+04 ± 1.56e+01
Bg3	−9008 ± 9.8
Bg4	2221 ± 5.2

Figure 2.17.: The distribution of the energy measured in the ECAL with second cuts applied to the transverse momentum in the calibration file.

2.4   Part 3: Measurement of the W-Boson mass

Having familiarized with particle identifications in the *ATLAS* experiment and having performed the calibration of the energy measurement, we are ready to conduct the main part of the experiment. There are two possibilities to choose from, either the measurement of the $W^{\pm}$ boson mass or the search for new physics – both use real *ATLAS* data. This choice had to be done on the first day already, as the calibration we did depended on this choice. We decided to measure the mass of the $W^{\pm}$ boson.

The analysis utilizes the decay modes $W^{\pm} \to e^{\pm} \overset{(-)}{\nu}_e$, where the $W^{\pm}$ boson might be produced in association with one or several jets. This will lead to undesired QCD background in the later measurements. We make use of the method explained in section 1.6.3, i.e. find the Jacobi peak position in the electron transverse momentum distribution to determine the $W^{\pm}$ boson mass. Here, one has to consider effects like the detector resolution, the $W^{\pm}$ boson's transverse momentum and the Breit-Wigner width of the $W^{\pm}$ boson, which all smear out the expected distribution. As a fit to the full electron p_T-distribution would be beyond the scope of this lab course, we use a simplified procedure to determine the position of the peak. This simplified procedure picks the el_pt value for which the histogram has half the entries compared to the peak bin (the so-called *half-maximum point*). It can be argued, that the smearing effects mentioned above act symmetrically and leave the position of the half-maximum point almost unchanged, thus making this point (located at $M_W/2$) a useful estimate of the Jacobi peak (cf. [1] for this paragraph).

We have several simulated data sets for the process $W^{\pm} \to e^{\pm} \overset{(-)}{\nu}_e$, as well as real ATLAS data on hand for this part of the analysis. The simulated data sets assume different masses of the $W^{\pm}$ boson in order to find a gauge curve of the nominal $W^{\pm}$ boson mass against the *half-maximum point*. Furthermore, we are provided a data set for the process $Z^0 \to e^- e^+$ to crosscheck our result of the gauge curve with the well known Z^0 boson mass. The *ROOT* script we use in this part is able to extract the unwanted QCD background by using background data obtained from the *ATLAS* experiement and also extract other background by using simulated data. Here, one has to further normalize/scale the QCD background, as the integrated luminosities do not match the number of events in the data set.

To begin the analysis, we use the following commands:

```
cd Wmass
.L Wenu.C+
Wenu w
```

These commands initialize a calibration object 'w' in a similar way to the calibration object for the Z^0 decays in the second part of the experiment. To verify the calibration of the electron momentum derived on the first day of the experiment, we successively use the commands

```
w.FitZee("")
w.FitZee("el_eta>-1.0 && el_phi<1.0 && pos_phi>-1.0 && pos_phi<1.0")
w.FitZee("el_phi>-2.0 && el_phi<2.0 && pos_phi>-2.0 && pos_phi<2.0")
w.FitZee("el_pt>40.0 && pos_pt>40.0")
```

to find the graphs depicted in figure 2.18. These commands work similar to the fit function in part 2 and use $Z^0 \rightarrow e^- e^+$ data from the *ATLAS* experiment to obtain the Z^0 boson mass. We will describe such graphs in more detail when considering the data for the $W^\pm$ decay, for now the output in the fitbox shall be sufficient.
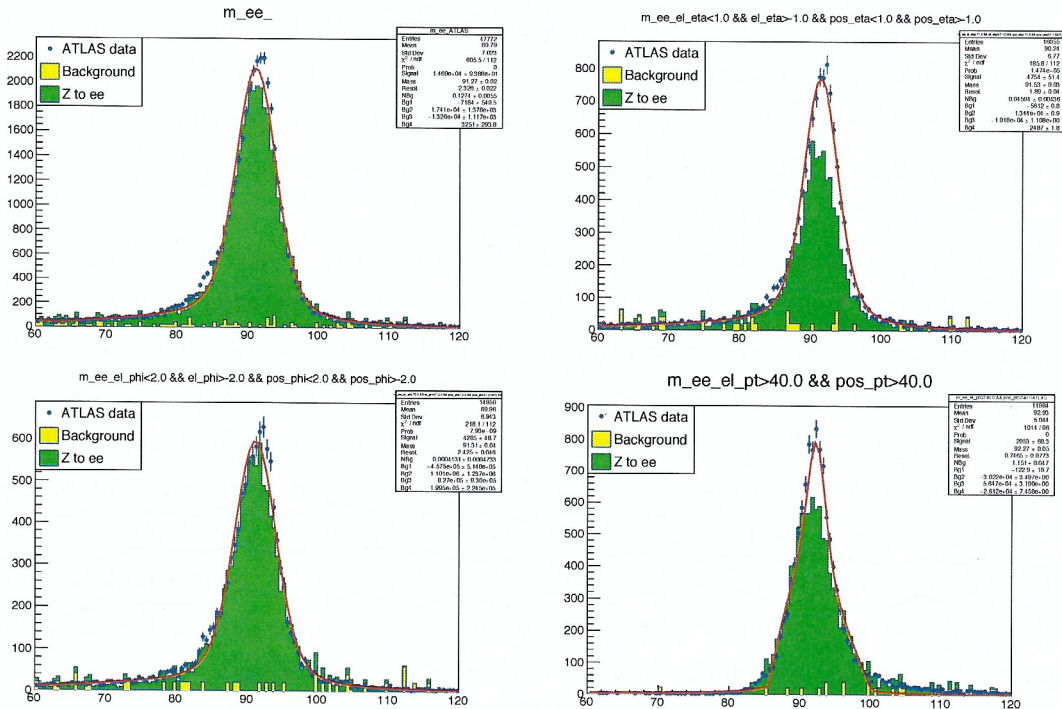
Figure 2.18.: The $Z^0 \rightarrow e^- e^+$ *ATLAS* data fitted with the calibrations found on the first day and cuts on η, ϕ and P_T.

The obtained Z^0 boson masses are in good correspondence to the nominal value $M_Z = (91.19 \pm 0.002)\,\text{GeV}$ (cf. [1]), and we conclude that the *ATLAS* data with the calibration we carried out reproduces the Z^0 boson mass to a good approximation.

After these steps, we use commands of the kind

```
w.PlotW("Variable", bin-number, lower boundary, upper boundarry, "cut
    selection")
```

in order to get *ATLAS* data of the desired variable plotted with a 'stack plot' from simulated data. In the following, we inspected the observables el_pt, el_etiso, njet, etmis and ptw, resulting in figure 2.19.
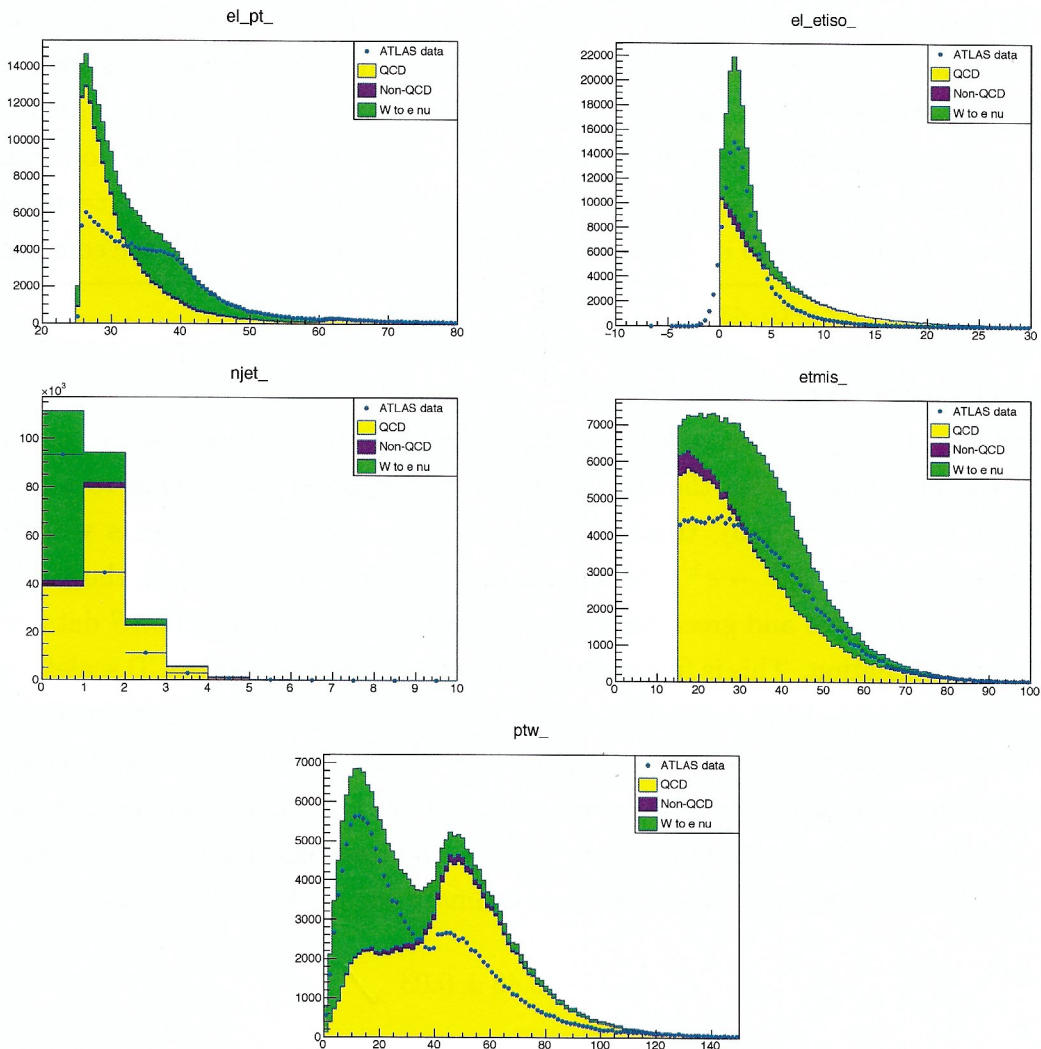
Figure 2.19.: The *ATLAS* data with simulated stack plots for the variables el_pt, el_etiso, njet, etmis and ptw.

The *ATLAS* data is depicted as the blue dots, while the data from simulations is represented as the yellow bars for the QCD background, the violet bars for non-QCD background stacked on top of these and the green bars for the process of interest $W^{\pm} \to e^{\pm}\overset{(-)}{\nu}_e$ further stacked on top of the other bars. Thus the name 'stack plot'. This will prove useful in determining the scaling factor for the QCD background, as we will discuss in the next paragraph.

If the QCD background was normalized appropriately, the green bars stacked on top of the yellow and violet ones in figure 2.19 should coincide with the blue data points from real *ATLAS* data to a good accuracy. To estimate the so-called QCD scalefactor S_{QCD}, it is commendable to inspect a kinematic region with a lot of QCD background and only a few events of interest (i.e. $W^{\pm} \to e^{\pm}\overset{(-)}{\nu}_e$). In that way, we can scale the simulated QCD background such that it coincides with the measured *ATLAS* data. Thence, we inspect the variable `ptw` with cuts on `njet` – the number of hadronic jets in the event. We start by looking at the constraint `njet==4` with only a few events remaining and iteratively go down to `njet==0` with 'only' non-QCD events in it. Setting the QCD scalefactor to 0.43 with the command

```
w.SetQCDScaleFactor(0.43)
```

we find figure 2.20 for said histograms.

For $n = 4, 3, 2$ jets, the yellow bars from the QCD background clearly coincide with the blue points from the *ATLAS* data. As expected when going to a lower number of jets ($n = 1, 0$), this is not the case anymore, as the events with the reaction of interest $W^{\pm} \to e^{\pm}\overset{(-)}{\nu}_e$ dominate over the QCD part. Instead, the stacked plot of yellow, violet and green bars coincides with the measured *ATLAS* data to a good approximation. This is further evidence that we found a good QCD scalefactor for the given data. Still, one would expect an uncertainty on the QCD scalefactor. To estimate this uncertainty, we slightly vary the QCD scalefactor and look at the resulting diagrams for the variables `el_pt`, `el_etiso`, `njet`, `etmis and ptw`. It turned out, that for an uncertainty of 0.03, the resulting diagrams were barely distinguishable from each other. We thus estimate our final QCD scale factor to

$$S_{\mathrm{QCD}} = 0.43 \pm 0.03$$

and find figure 2.21 upon replotting the observables from figure 2.19.

Note here, that usually one would also have to find a signal scale factor, which fortunately already has a good preset in our case.
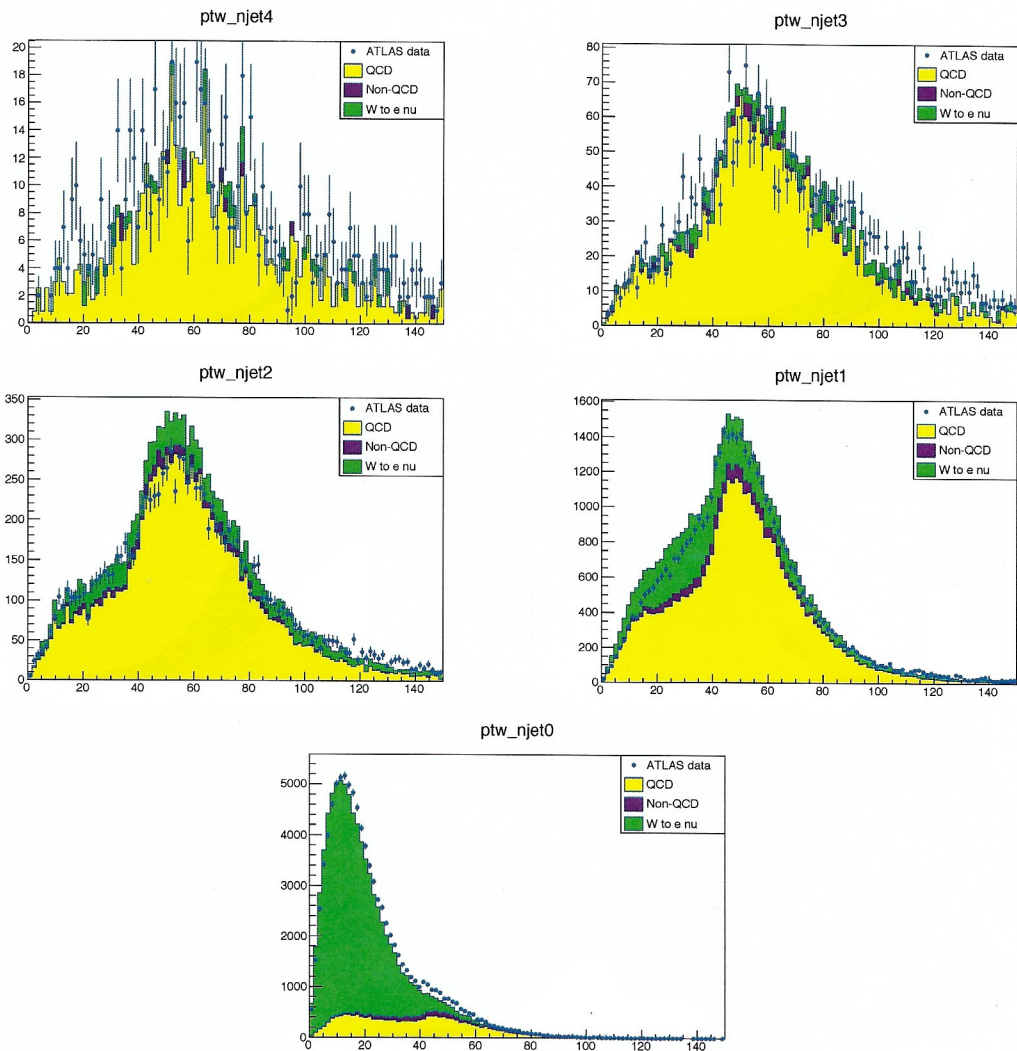
Figure 2.20.: The histograms for the observable `ptw` with the constraints `njet==4`, `njet==3`, `njet==2`, `njet==1` and `njet==0`.
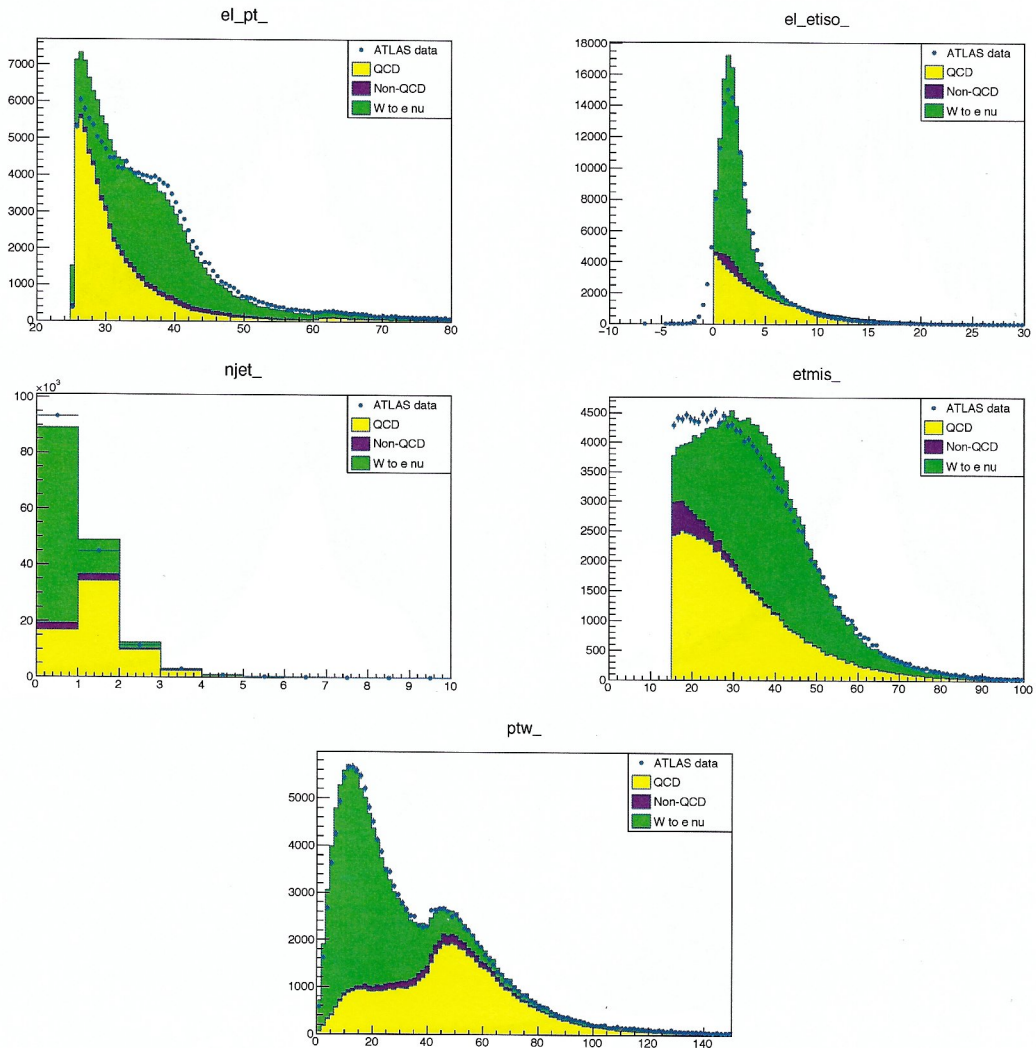
Figure 2.21.: The *ATLAS* data with simulated stack plots for the variables el_pt, el_etiso, njet, etmis and ptw and an applied QCD scalefactor of $S_{\mathrm{QCD}} = 0.43$.

Having obtained an appropriate normalization for the QCD background, we turn to the measurement of the $W^{\pm}$ boson mass and select a suitable data set. This data set should contain only a small amount of (QCD) background. To that end, we define suitable cuts on the data set, where it is important that the P_T-spectrum features a prominent Jacobi peak. After trying out several different cuts, we decided for the combinations `el_ptw < 25.0, njet < 1 and etmis > 20.0`, leading to figure 2.22 for the distribution of the variable `el_pt`.
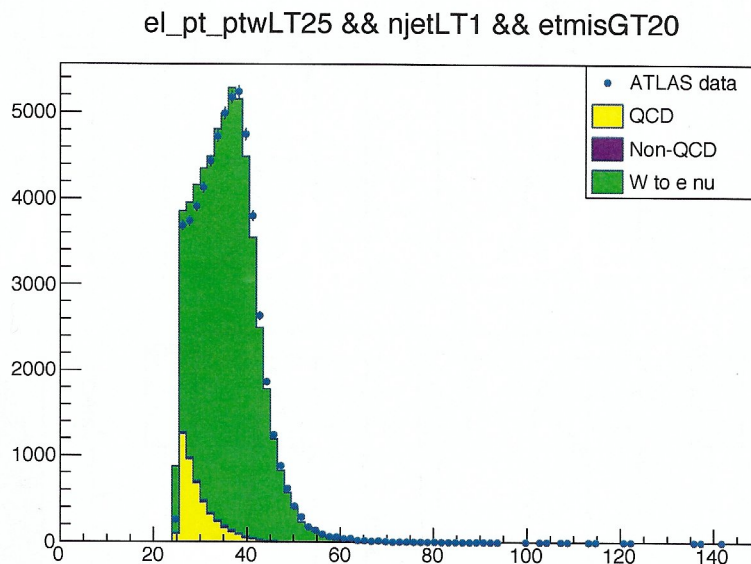
Figure 2.22.: The histogram of the observable `el_pt` with an applied QCD scale-factor of $S_{\mathrm{QCD}} = 0.43$ and the cuts `el_ptw < 25.0, njet < 1, etmis > 20.0`.

The cut on `el_ptw` restricts the transverse momentum P_T of the $W^{\pm}$ boson to small values, as a higher transverse momentum means the production of more hadronic jets. The cut on `njet` further aggravates the restriction on the number of jets. The cut on the missing transversal energy $E_{\mathrm{T\text{-}mis}}$ cuts on the events with non-vanishing missing transversal energy, i.e. with a neutrino leaving the detector. There was no reason to further apply a cut like e.g. `el_pt > 20` on the transverse momentum of the electron, as the distribution of `el_pt` only starts at $P_T \gtrsim 25$ (see figure 2.22). In order to fix the desired cuts for all subsequent fits, we use the following command:

```
w.SetCutSelection("el_ptw < 25.0 && njet < 1 && etmis > 20.0")
```

The cuts determined above and the QCD-background scale factor are applied onto Monte-Carlo generated simulated $W^{\pm} \to e^{\pm} \overset{(-)}{\nu}_{e}$ events with the $W^{\pm}$ boson mass assumed as $M_W^{MC} = 75\,\text{GeV}$, $78\,\text{GeV}$, $79\,\text{GeV}$, $80\,\text{GeV}$, $81\,\text{GeV}$, $82\,\text{GeV}$ and $85\,\text{GeV}$. A predefined fit in the range from $28\,\text{GeV}$ to $60\,\text{GeV}$ is used to determine the position of the half-maximum (HM), where the results are shown in figure 2.23.
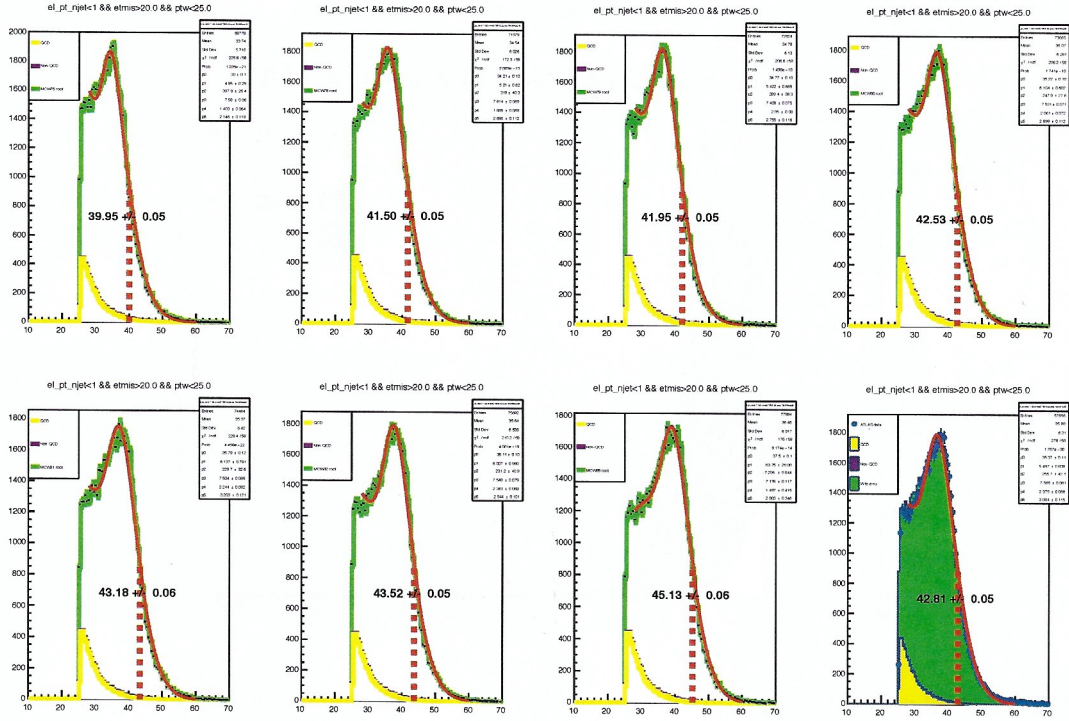
Figure 2.23.: Half-maximum fits for different Monte Carlo masses and real *ATLAS* data for the plot in the lower right corner. The fit is applied in a range from $28\,\text{GeV}$ to $60\,\text{GeV}$.

Due to the smearing effects mentioned in 1.6.3, this can be identified as the location of the Jacobi Peak up to first order. The values for HM can be found in table 2.3. The uncertainty on the real position of the peak is corrected by creating a *gauge curve* relating the half-maximum position to the mass of the $W^{\pm}$ boson in the generated data.

In the following, the influence of the used methods is studied to define a systematic error. Therefore, the used cuts, background scale factor and fit range are changed slightly respectively. Then, the fit procedure is applied again, where the figures can be found in the appendix, figures B.1-B.9. An error is estimated by taking the difference of these values for HM to the values in table 2.3 for each mass and taking the median afterwards because of its robustness to outliers.

M_W^{MC} [GeV]	HM [GeV]
75	39.95±0.05
78	41.50±0.05
79	41.95±0.05
80	42.53±0.05
81	43.18±0.06
82	43.52±0.05
85	45.13±0.06

Table 2.3.: Half-maximum position of the Monte Carlo generated data samples. Only the statistical error on HM is shown, a common systematic error of 0.13 GeV must be added.

Table 2.4 shows the found differences. Errors from QCD background-scaling and cuts on the number of jets are neglectable. From these values, a systematic error is found by taking the arithmetic mean, yielding

$$(\Delta HM)_{\mathrm{sys}} = 0.13 \,\mathrm{GeV}, \qquad (2.1)$$

which is now applied to all samples.

Changed Parameter		Difference [GeV]
	min 32 GeV	0.06
fit region	min 25 GeV	0.05
	max 50 GeV	0.1
$\not{E}_T$	> 10 GeV	0.14
	> 30 GeV	0.25
p_T^W	< 20 GeV	0.19

Table 2.4.: The effect on HM upon changing the given parameters.

For the gauge curve, the values for $HM \pm (\Delta HM)_{\mathrm{stat}} \pm (\Delta HM)_{\mathrm{sys}}$ are plotted against the masses of the MC dataset. Since the Jacobi peak position is proportional to the mass, a linear function is fitted to the data.

$$M_W = m(HM - \overline{HM}) + n \qquad (2.2)$$

$\overline{HM}$ is chosen to minimize the correlation between m and n. Figure 2.24 shows the resulting gauge curve.
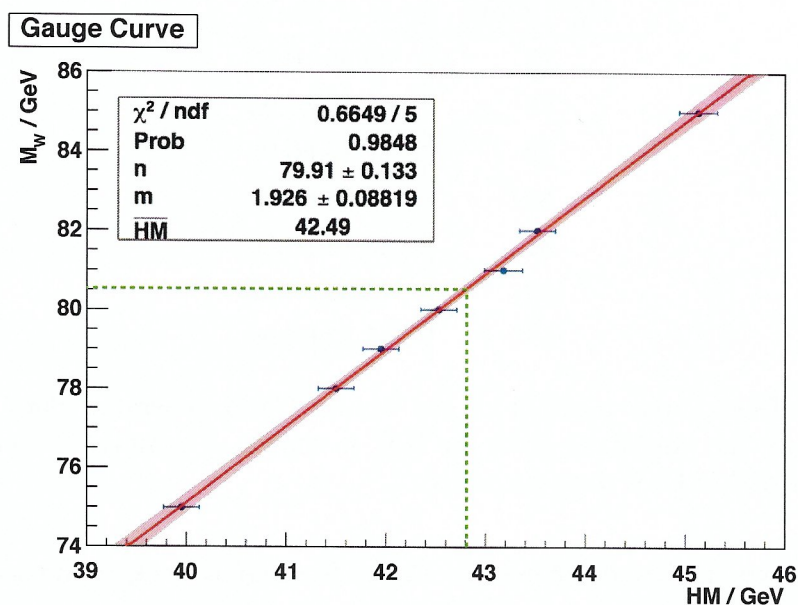
Gauge Curve

Figure 2.24.: The resulting gauge curve for the $W^{\pm}$ boson masses of the MC datasets against the HM. The red shaded area shows the error region of the fit and the green line denotes the position of the 'real' $W^{\pm}$ boson.

The quality of the gauge curved is now checked by using the half-maximum method for the $Z^0 \to e^- e^+$ sample, as seen in figure 2.25.
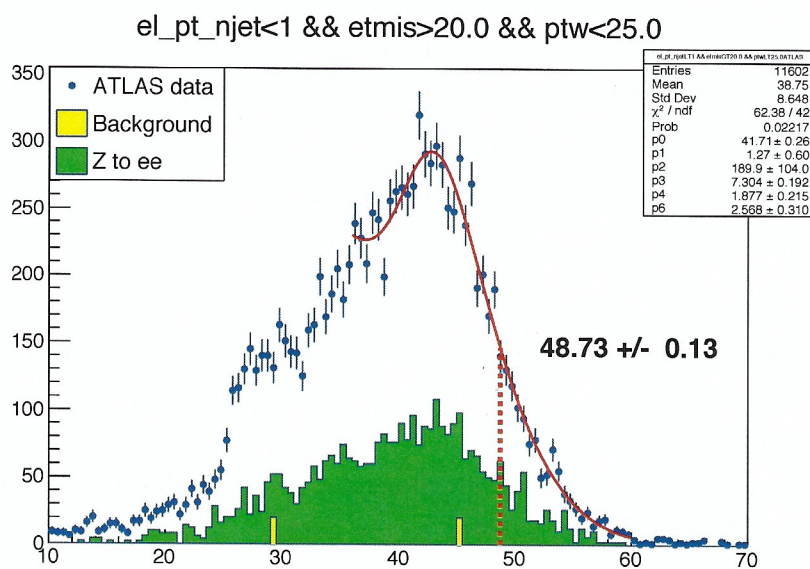

Figure 2.25.: Determination of HM in the transverse momentum spectrum of electrons in the decay $Z^0 \to e^- e^+$.

The cut on the missing transverse momentum was adopted from the $W^{\pm} \to e^{\pm} \overset{(-)}{\nu}_e$ events, but is wrong here as we do not expect a missing transverse momentum in

$e^- e^+$ pair production. A half-maximum value of

$$HM_Z = (48.73 \pm 0.13_{\text{stat}} \pm 0.13_{\text{sys}})\,\text{GeV}$$

is found and using the gauge curve eq. (2.2), we find a mass of

$$M_Z = (91.93 \pm 0.61_{\text{stat}} \pm 0.61_{\text{sys}})\,\text{GeV} = (91.93 \pm 0.87_{\text{tot}})\,\text{GeV}.$$

Here, the statistic and systematic errors are calculated separately by gaussian error propagation, since the covariance between m and n is neglectable ($\sigma_{mn} \approx 10^{-7}\,\text{GeV}$). As the value is in accordance with the literature value of $M_Z^{\text{lit}} = 91.1876 \pm 0.0021\,\text{GeV}$ (cf. [1]) in one standard deviation, no further systematic error is used.

With the measured value $HM = (42.81 \pm 0.05_{\text{stat}} \pm 0.13_{\text{sys}})\,\text{GeV}$ of the real $W^{\pm}$, its mass can be determined to be

$$M_W = (80.53 \pm 0.16_{\text{stat}} \pm 0.28_{\text{sys}})\,\text{GeV} = (80.53 \pm 0.33_{\text{tot}})\,\text{GeV}.$$

This is really small, how did you calculate it?

Note here, that the value for HM is dependent on the choice of the fitrange, what eventually leads to a large systematic error. Thus, the systematic error could be reduced by performing a fit to the whole P_T-distribution, as suggested in [1]. The value for HM is further remarkably dependent on the choice of the cuts on `ptw` and `etmis`. An improvement on the systematic error regarding these values could not be found by us.

3 Conclusion

In this experiment, we used the event display of the program *ATLANTIS* to identify different events in the detector and determine the energy-over-momentum ratio from electron events, as well as the photon conversion probability from photon events. We found, that the energy-over-momentum ratio is $E/P \approx 1.13$ and the conversion probability for photons $P_{\gamma\text{-conv}} \approx 0.18$. We also calibrated the electromagnetic calorimeter using electron data, such that we regard the varying energy yields of the calorimeter, defect calorimeter modules and the variable distances the particles travel before being measured. We found cuts on the variables `el_eta`, `el_phi` and `el_pt` such that we find the Z^0 boson mass $M_Z = (91.22 \pm 0.01)\,\text{GeV}$ with a resolution of $(2.291 \pm 0.017)\,\text{GeV}$. Doing more iterations on `el_eta`, or choosing a finer segmentation, one could achieve better results here. For our purpose, the achieved accuracy was enough.

In the main part of this experiment, we measured the $W^\pm$ boson mass using real *ATLAS* data for the process $W^\pm \to e^{\pm}\overset{(-)}{\nu}_e$. To this end, we determined a scaling factor for the QCD background in the *ATLAS* data to $S_{\text{QCD}} = (0.43 \pm 0.03)$ and cuts in order to eliminate QCD events as follows: `el_ptw < 25.0`, `njet < 1` and `etmis > 20.0`. Afterwards, we used the Jacobi peak method for Monte Carlo generated data with differently assumed $W^\pm$ boson masses to create a gauge curve, giving the dependency of the half-maximum point against the nominal $W^\pm$ boson mass. For the real *ATLAS* data, we then found $M_W = (80.53 \pm 0.16_{\text{stat}} \pm 0.28_{\text{sys}})\,\text{GeV} = (80.53 \pm 0.33_{\text{tot}})\,\text{GeV}$ for the $W^\pm$ boson and as a crosscheck $M_Z = (91.93 \pm 0.61_{\text{stat}} \pm 0.61_{\text{sys}})\,\text{GeV} = (91.93 \pm 0.87_{\text{tot}})\,\text{GeV}$ for the Z^0 boson. These values coincide with the literature values from [1] within one standard deviation, being $M_W = (80.40 \pm 0.03)\,\text{GeV}$ and $M_Z = (91.19 \pm 0.002)\,\text{GeV}$. The remarkable dependence of these values on the fitrange, the values for the transverse momentum of the $W^\pm$ boson and the missing transverse momentum yields a large systematic error, which could further be improved by performing the fit to the P_T-distribution as suggested in [1].

A   Calibration File 'ElecCalib.C'

```
if (eta<2.5 && eta>2.25) energy = energy * 91.19/88.39 * 91.19/90.72;
  else if (eta<2.25 && eta>2.0) energy = energy * 91.19/88.85 *
      91.19/90.76;
  else if (eta<2.0 && eta>1.75) energy = energy * 91.19/90.51 *
      91.19/91.58;
  else if (eta<1.75 && eta>1.45) energy = energy * 91.19/89.59 *
      91.19/91.27;
  else if (eta<1.45 && eta>1.15) energy = energy * 91.19/89.4 *
      91.19/91.06;
  else if (eta<1.15 && eta>0.90) energy = energy * 91.19/89.39 *
      91.19/91.12;
  else if (eta<0.90 && eta>0.65) energy = energy * 91.19/89.57 *
      91.19/91.09;
  else if (eta<0.65 && eta>0.40) energy = energy * 91.19/89.92 *
      91.19/91.32;
  else if (eta<0.40 && eta>0.15) energy = energy * 91.19/90.04 *
      91.19/91.35;
  else if (eta<0.15 && eta>-0.1) energy = energy * 91.19/89.96 *
      91.19/91.34;
  else if (eta<-0.1 && eta>-0.35) energy = energy * 91.19/89.98 *
      91.19/91.36;
  else if (eta<-0.35 && eta>-0.60) energy = energy * 91.19/89.98 *
      91.19/91.39;
  else if (eta<-0.60 && eta>-0.85) energy = energy * 91.19/89.71 *
      91.19/91.19;
  else if (eta<-0.85 && eta>-1.10) energy = energy * 91.19/89.48 *
      91.19/91.13;
  else if (eta<-1.10 && eta>-1.45) energy = energy * 91.19/89.45 *
      91.19/91.08;
  else if (eta<-1.45 && eta>-1.80) energy = energy * 91.19/89.84 *
      91.19/91.42;
```

```
else if (eta<-1.80 && eta>-2.05) energy = energy * 91.19/89.92 *
    91.19/91.38;
else if (eta<-2.05 && eta>-2.25) energy = energy * 91.19/88.81 *
    91.19/90.91;
else if (eta<-2.25 && eta>-2.50) energy = energy * 91.19/87.78 *
    91.19/90.34;


if (phi>2 && phi<3.5) energy = energy * 91.19/91.25 * 91.19/91.21;
else if (phi>1 && phi<2) energy = energy * 91.19/91.33 * 91.19/91.25;
else if (phi>0 && phi<1) energy = energy * 91.19/91.21 * 91.19/91.2;
else if (phi>-1 && phi<0) energy = energy * 91.19/91.2 * 91.19/91.17;
else if (phi>-2 && phi<-1) energy = energy * 91.19/91.25 * 91.19/91.16;
else if (phi>-3.5 && phi<-2) energy = energy * 91.19/91.2 * 91.19/91.18;


if (pt>0 && pt<20) energy = energy * 91.19/89.48 * 91.19/90.12;
else if (pt>20 && pt<30) energy = energy * 91.19/90.19 * 91.19/90.94;
else if (pt>30 && pt<35) energy = energy * 91.19/90.57 * 91.19/90.95;
else if (pt>35 && pt<40) energy = energy * 91.19/90.7 * 91.19/90.89;
else if (pt>40 && pt<45) energy = energy * 91.19/91.25 * 91.19/91.1;
else if (pt>45 && pt<50) energy = energy * 91.19/92.2 * 91.19/91.64;
else if (pt>50 && pt<60) energy = energy * 91.19/92.05 * 91.19/91.81;
else if (pt>60 && pt<80) energy = energy * 91.19/91.91 * 91.19/91.77;
else if (pt>80) energy = energy * 91.19/91.71 * 91.19/91.74;
```

B Figures
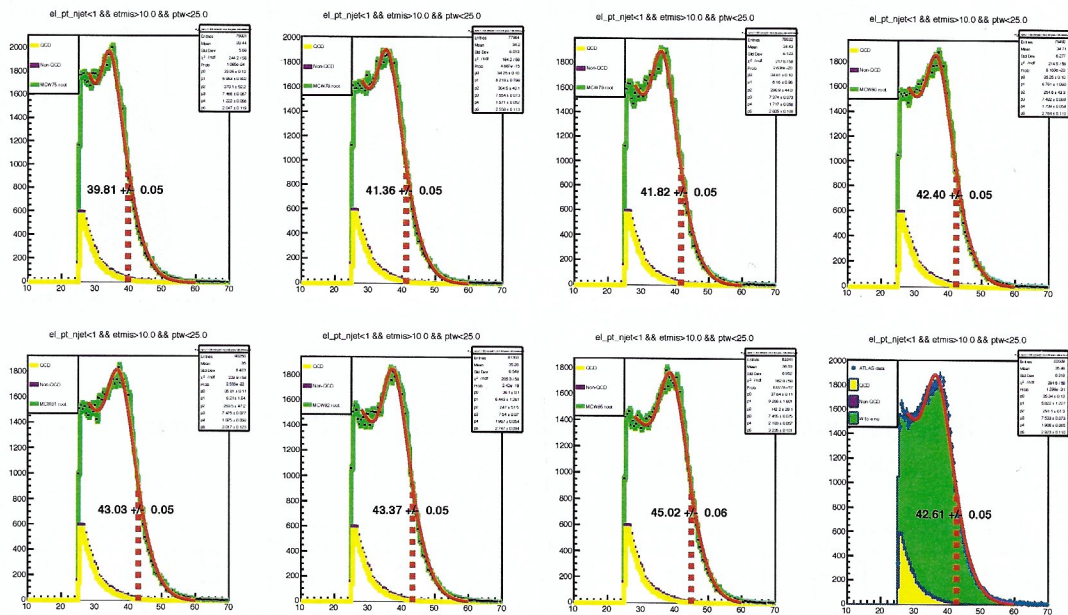
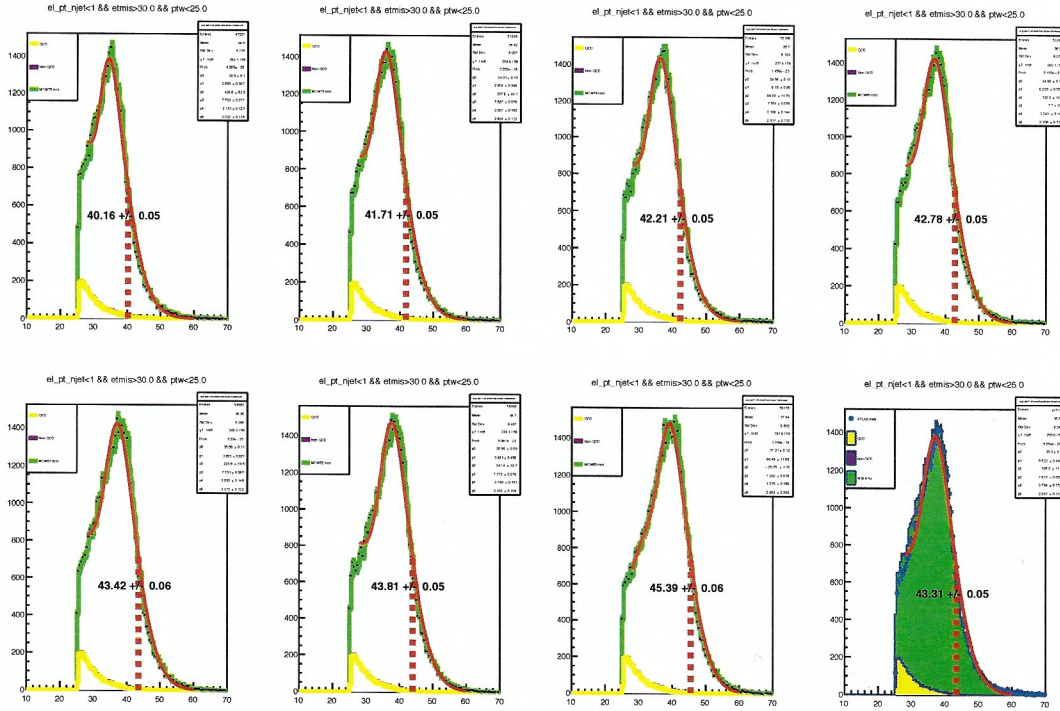Figure B.1.: Half-maximum fits for Monte Carlo and real *ATLAS* data. Here, the cut `etmis>10` is set.

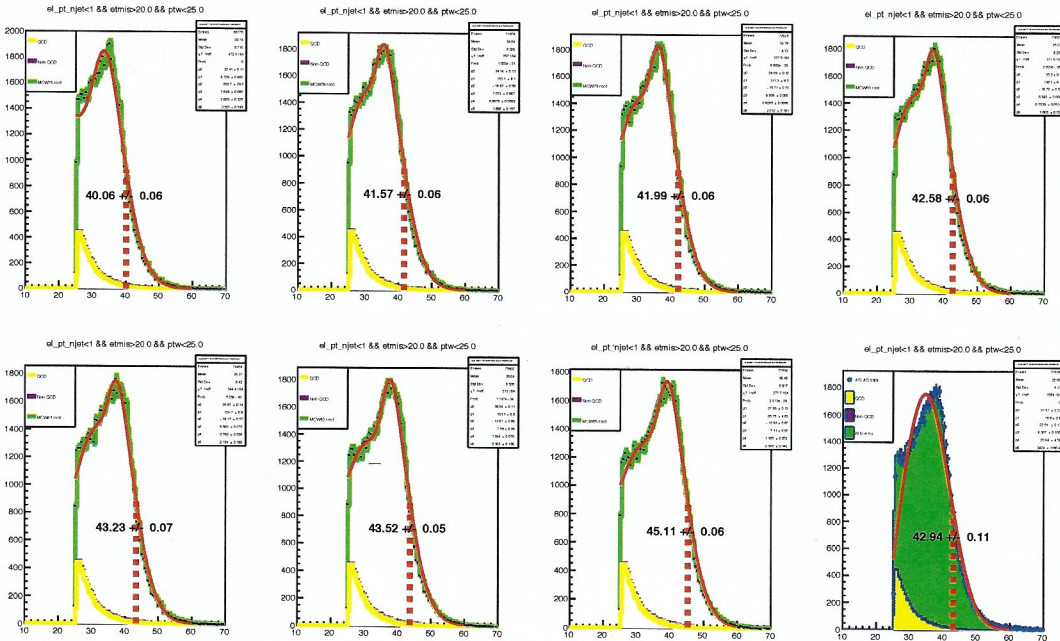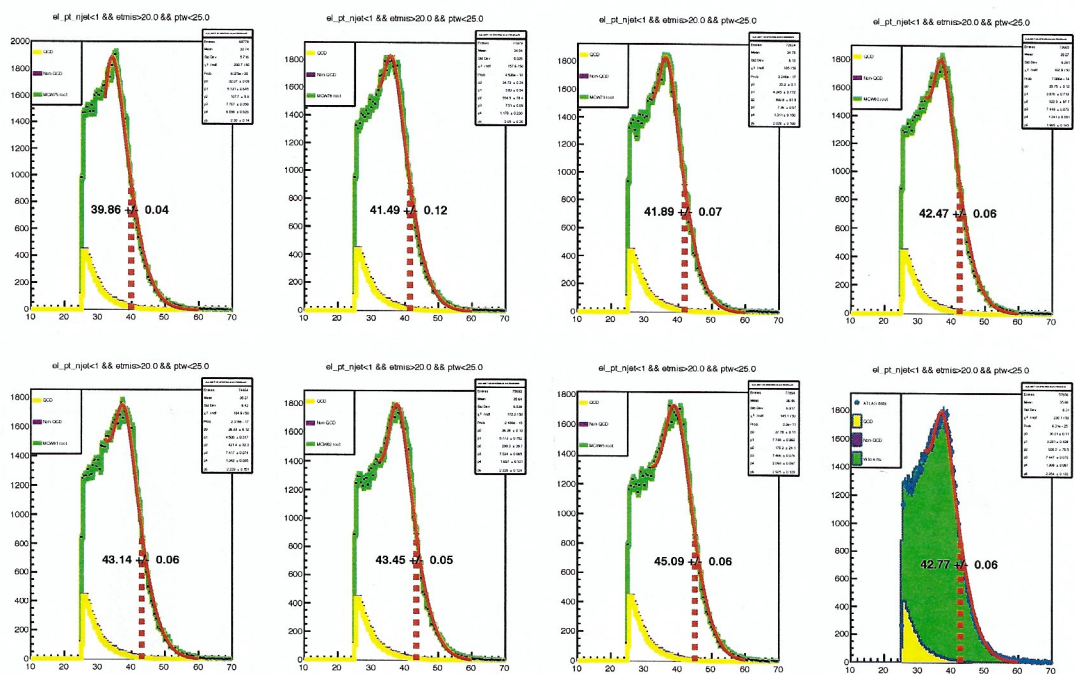Figure B.2.: Half-maximum fits for Monte Carlo and real *ATLAS* data. Here, the cut `etmis>30` is set.

Figure B.3.: Half-maximum fits for Monte Carlo and real *ATLAS* data. Here, the lower fit bound is set to 25.

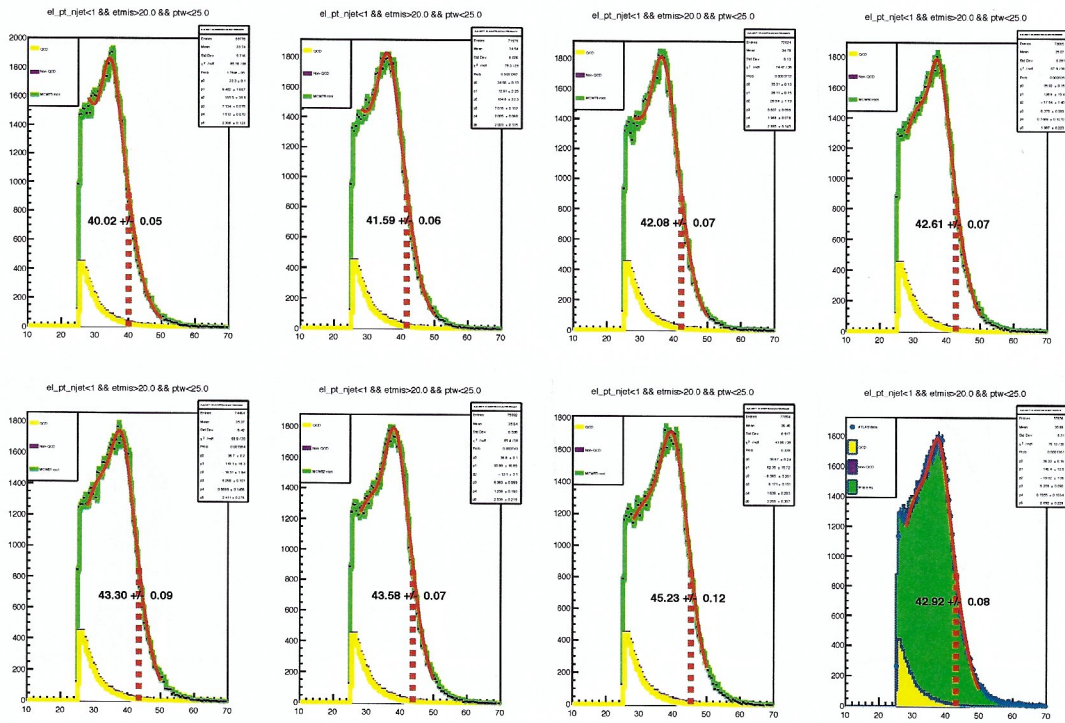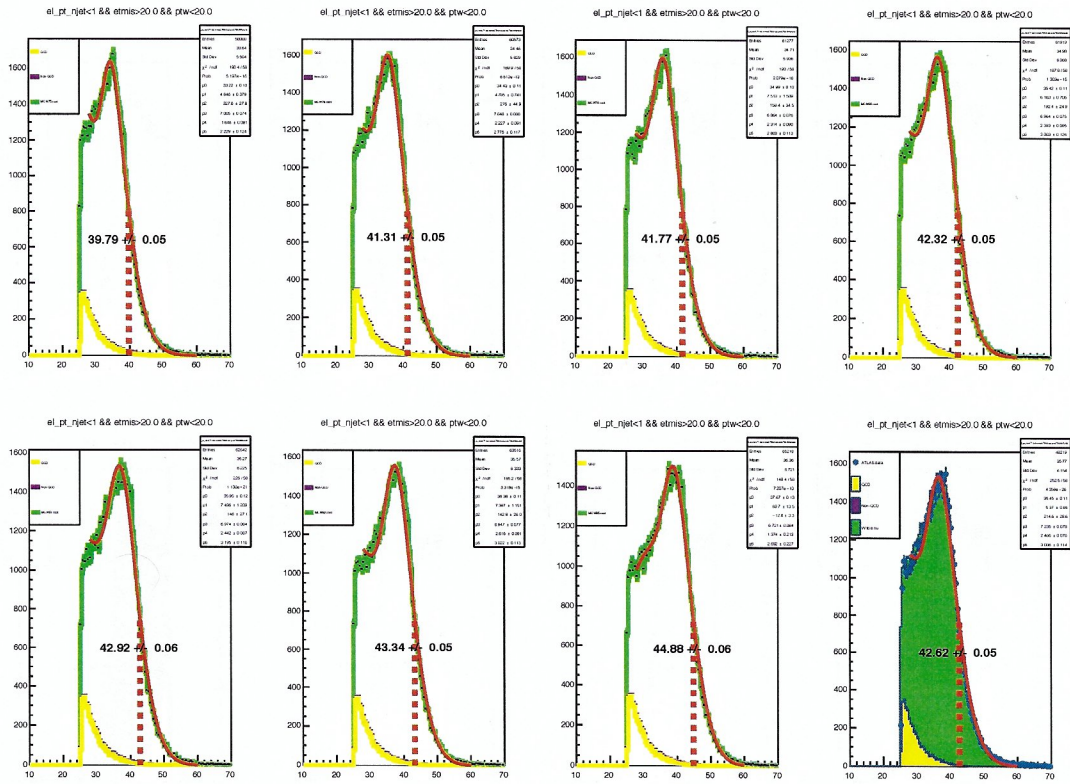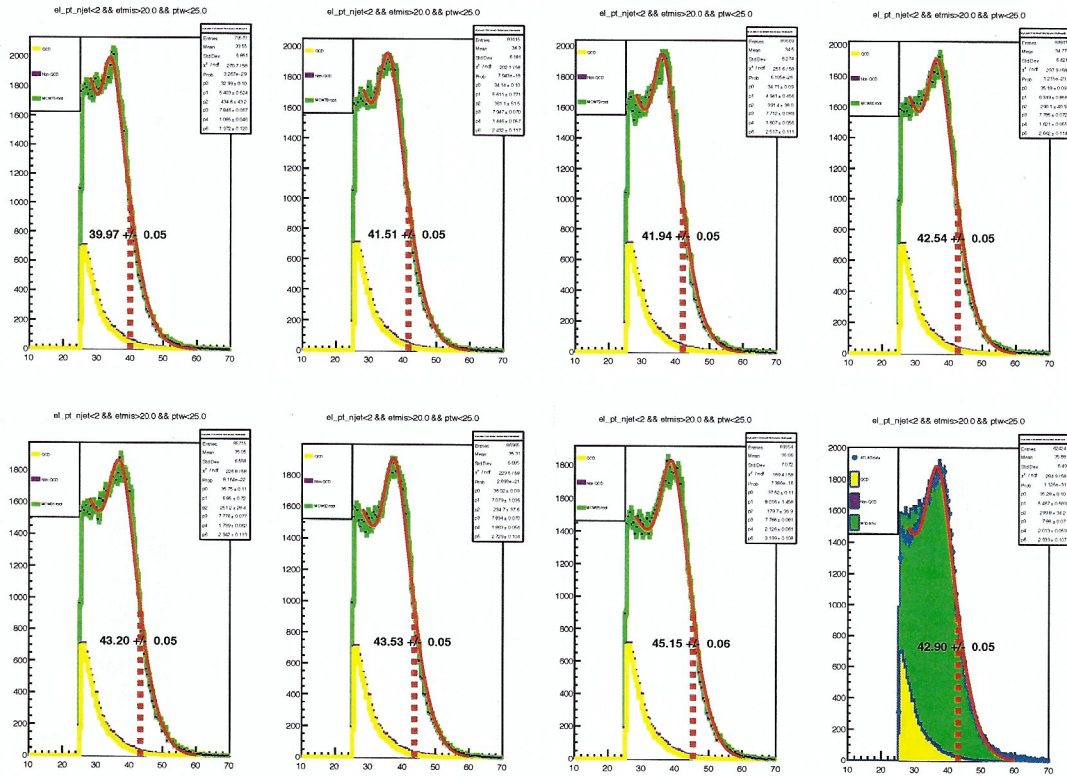Figure B.4.: Half-maximum fits for Monte Carlo and real *ATLAS* data. Here, the lower fit bound is set to 32.

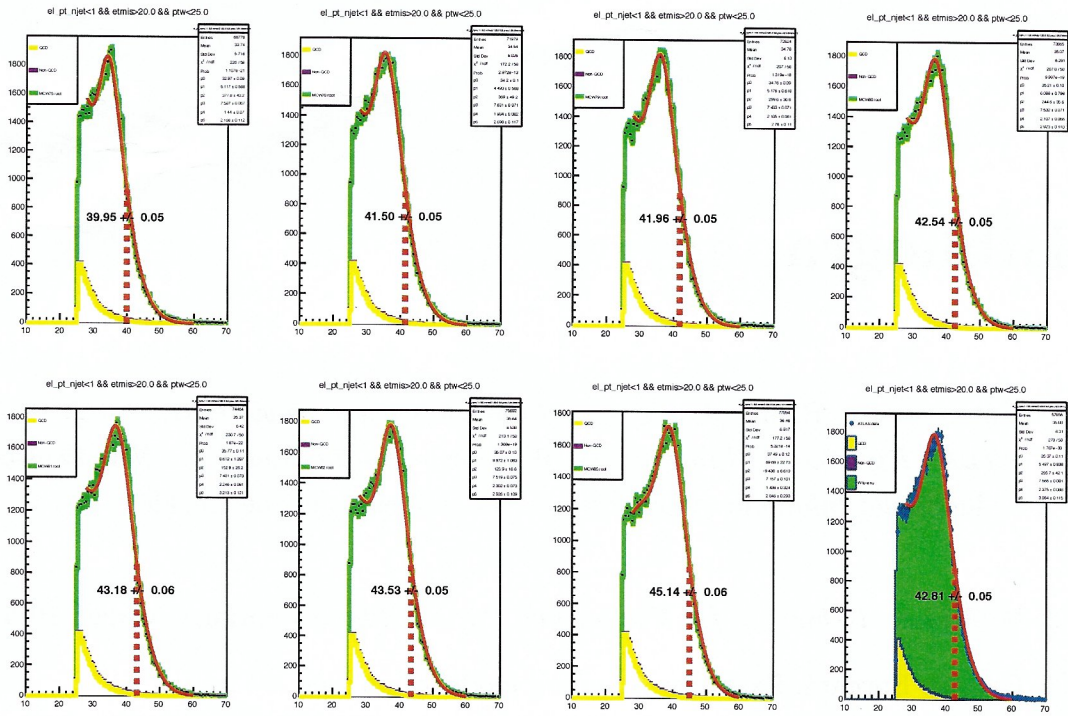Figure B.5.: Half-maximum fits for Monte Carlo and real *ATLAS* data. Here, the upper fit bound is set to 50.

Figure B.6.: Half-maximum fits for Monte Carlo and real *ATLAS* data. Here, the cut `ptw<20` is set.

Figure B.7.: Half-maximum fits for Monte Carlo and real *ATLAS* data. Here, the
cut `njet<2` is set.

Figure B.8.: Half-maximum fits for Monte Carlo and real *ATLAS* data. Here, the QCD scalefactor is set to 0.40.
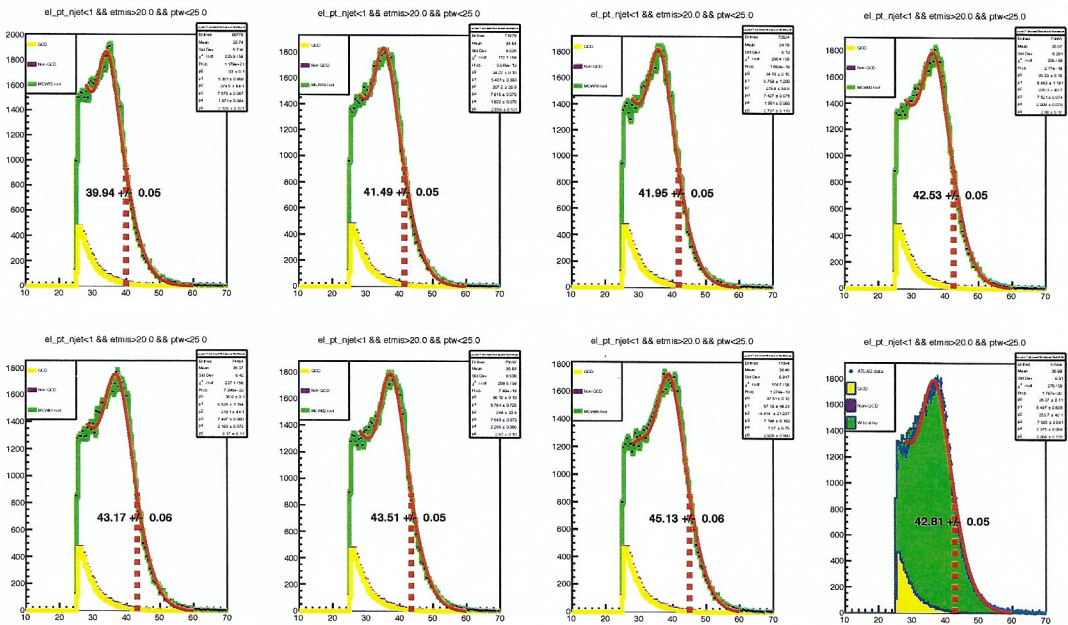

Figure B.9.: Half-maximum fits for Monte Carlo and real *ATLAS* data. Here, the QCD scalefactor is set to 0.46.

Bibliography

[1] University of Bonn. *Advanced Laboratory Course physics601, E214: The ATLAS Experiment (Properties of W Bosons and the Search for New Physics) – Additional Information handed out.* And references in this booklet.

[2] W. R. Leo *Techniques for Nuclear and Particle Physics* Springer Verlag, 1987

[3] Carsten Burgard. Example: Standard model of physics. `http://www.texample.net/tikz/examples/model-physics`

[4] M. Drees, R. M. Godbole and P. Roy. *Theory and Phenomenology of Sparticles.* World Scientific Publishing Co. Pte. Ltd., 2004.

[5] M. E. Peskin and D. V. Schroeder. *An Introduction to Quantum Field Theory.* Westview Press, 2016.

[6] V. Büge, A. Ghezzi and et. al., *Prospects for the precision measurement of the W mass with the CMS detector at the LHC.* Journal of Physics G: Nuclear and Particle Physics (2007). `http://stacks.iop.org/0954-3899/34/i=5/a=N02`

[7] University of Bonn. *Advanced Laboratory Course (physics601), Description of Experiments: E214 ATLAS.* (Blue booklet). May 2012.

[8] Wikipedia: Propagation of Uncertainty. `https://en.wikipedia.org/wiki/Propagation_of_uncertainty.`

[9] C. Patrignani et al. (Particle Data Group), Chin. Phys. C, 40, 100001 (2016) and 2017 update.

[10] RWTH Aachen, Thomas Hebbeker. Vorbereitungskurs F-Praktikum B (Physik) `https://web.physik.rwth-aachen.de/~hebbeker/lectures/stat_fprakt_1.pdf.`

[11] University of Colorado, Minhyea Lee. PHYS2150 Experimental Physics, Spring 2018 `https://www.colorado.edu/physics/phys2150/phys2150_sp14/phys2150_lec4.pdf.`